Evidence for Noachian flood volcanism in Noachis Terra, Mars, and the possible role of Hellas impact basin tectonics

A. D. Rogers[1] and A. H. Nazarian[1]

Received 21 January 2013; revised 16 April 2013; accepted 20 April 2013.

[1] Spectral and imaging data sets from Mars Reconnaissance Orbiter and Mars Odyssey, as well as spectral and topographic data from Mars Global Surveyor, are used to understand the origin of in-place rock units found in the intercrater plains and Hellas circumferential graben floors of Noachis Terra, Mars. The rocky units are interpreted as effusive volcanic plains on the basis of broad areal extent, structural competence, association with topographic lows, distinct mineralogy from regolith, and lack of sedimentary textures or minerals associated with aqueous processes. Some rocky expanses contain at least two compositionally distinct units. The relatively light-toned unit exhibits a higher plagioclase/pyroxene ratio than the lower, dark-toned unit. Both units exhibit ~10% olivine enrichment compared to surrounding regolith. These units are heavily degraded and exhibit crater model ages between ~3.80 and 4.0 Ga, making these some of the oldest preserved volcanic plains accessible by remote sensing. They are found in association with Hellas ring structures, where the westward extent of these rocky units is limited to the outermost ring structure. Fracturing associated with the Hellas impact may have enabled magmas to ascend from the base of the crust in the circum-Hellas region. Identification of these units as volcanic materials extends previous estimates for volume of outgassed volatiles. Though the estimated volcanic volume increase is minor, the local effects could have been significant. The role of multi-ring impact basins in providing a spatial control on Martian highlands volcanism and subsurface mineralization may have been underestimated in the past.

Citation: Rogers, A. D., and A. H. Nazarian (2013), Evidence for Noachian flood volcanism in Noachis Terra, Mars, and the possible role of Hellas impact basin tectonics, *J. Geophys. Res. Planets*, *118*, doi:10.1002/jgre.20083.

1. Introduction

[2] Constraining the origin, style, and timing of volcanic activity on Mars is important for understanding its thermal evolution and climate history. Outside of the Tharsis province, major areas of known volcanic origin in the ancient Martian highlands include Syrtis, Hesperia, and Malea Plana, which are usually mapped as Late Noachian to early Hesperian in age [e.g., *Nimmo and Tanaka*, 2005] and are characterized by compressional features known as wrinkle ridges. In contrast, volcanism during the earliest part of Martian history is less well constrained because of confounding influences from impact, aeolian, fluvial, and ice-driven processes. Much of the Noachian surface of Mars consists of heavily degraded craters and intercrater plains. These intercrater plains have been previously interpreted as a mixture of volcanics, sediments, and impact breccias of unknown proportions [*Malin*, 1976; *Tanaka et al.*, 1988].

[1]Department of Geosciences, Stony Brook University, Stony Brook, New York, USA.

Corresponding author: A. D. Rogers, Department of Geosciences, Stony Brook University, 255 Earth and Space Sciences Building, Stony Brook, NY 11794-2100 USA. (Deanne.Rogers@stonybrook.edu)

2169-9097/13/10.1002/jgre.20083

[3] Much of the Martian surface is dominated by unconsolidated material [*Christensen and Moore*, 1992] which hinders compositional and textural analyses of large expanses of crust-forming material. Access to in-place, crust-forming materials is needed to unravel the processes which contributed to the evolution of the crust. Infrared data from the Mars Odyssey Thermal Emission Imaging System (THEMIS) have been used to successfully locate rare expanses of exposed bedrock [*Rogers et al.*, 2009; *Edwards et al.*, 2009; *Rogers and Fergason*, 2011]. In Noachis Terra/Mare Serpentis, a region where many of these exposures are spatially concentrated, *Rogers et al.* [2009] showed that these rocky units exhibit an enrichment (~10%) in olivine and/or pyroxene relative to low thermal inertia, sediment-dominated plains material in the region. Recent global analyses of Mars Express Observatoire pour la Minéralogie, l'Eau, lesGlacesetl'Activité (OMEGA) data confirm olivine enrichment in these plains [*Ody et al.*, 2012a, 2012b]. The crisp, rugged appearance of these units suggests a resistant, structurally competent unit compared to the subdued appearance of the surrounding low thermal inertia terrain (Figure 1). The resistant morphology and distinct mineral composition led *Rogers et al.* [2009] to speculate that the units were likely volcanic in origin. The presence of multiple units within the bedrock was suggested by *Rogers et al.* [2009]; however, because of the limited high-quality IR data and supporting high-resolution imagery at the time of that study, it was difficult to pursue the distribution and details of those units.

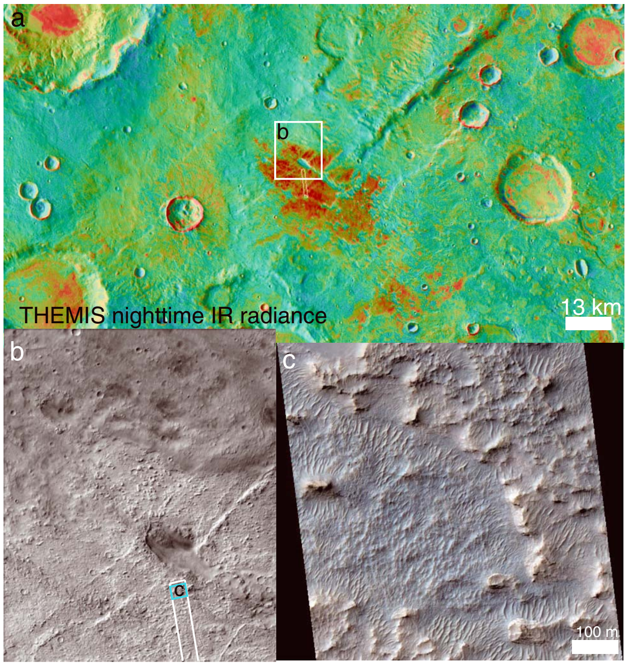

Figure 1. Introduction to the nighttime infrared and high-resolution views of rocky exposures in Noachis Terra. (a) Colorized THEMIS nighttime IR radiance mosaic draped over THEMIS daytime radiance mosaic. Warmer colors indicate higher radiances and warmer nighttime surface temperatures; quantitative radiance values are not available because the images used in the mosaic have been normalized to one another to produce a smooth image. The intercrater plain rocky unit is in the center of the image (38.6°E, −23.2°S); maximum THEMIS thermal inertia for this exposure is 575 $J\,m^{-2}\,K^{-1}\,s^{-0.5}$. (b) Portion of CTX image P17_007597_1568_XN_23S321W, which contains the rocky unit and surrounding low-TI plains material. Note NE-SW trending linear ridges (likely faults) that produced ~50–100 m vertical relief variations within the rocky exposure and surroundings. (c) Portion of HiRISE image PSP_007597_1565_COLOR, which shows pits, mesas, knobs, and bed forms. Additional high-resolution views of rocky exposures are shown in Figure 8.

[4] Here we use new spectral and imaging data sets from Mars Reconnaissance Orbiter (MRO) and Mars Odyssey (MO) as well as spectral and topographic data from Mars Global Surveyor (MGS) to better understand the origin of these units and the relative timing of volcanic and tectonic events. We also extend the original study region of *Rogers et al*. [2009] by a factor of ~8 to better understand the extent of similar surfaces. We present new evidence that many of the rocky expanses in this region were created by effusive volcanism in mid-Noachian to Late Noachian time period and have experienced extensive modification, burial, and exhumation in some places. We show a likely relationship to crustal fracturing and extension related to post-impact development of Hellas Basin. Finally, we discuss the implications of these findings for ancient Martian climate and habitability.

2. Study Region and Previous Work

[5] The study region (Figure 2), which spans from 350°E to 70°E, 0°S to −40°S, is dominated by Noachian and Hesperian-aged units [*Greeley and Guest*, 1987]. It includes the classic albedo features Noachis Terra, Mare Serpentis, Pandorae Fretum, and portions of Terra Sabea, Sinus Meridiani, and Sinus Margaritifer. Much of the region is characterized by low (<0.15) albedo, heavily cratered terrain which has been dissected by immature fluvial networks in many places. Less dominant are interspersed early Hesperian-aged smooth or ridged plains.

[6] The study region includes some of the thickest crust on Mars and is partially composed of high-standing annulus around the Hellas Basin, which likely represents excavated crust ejected during the Hellas impact event [*Smith et al*., 1999; *Zuber et al*., 2000; *Neumann et al*., 2004] (~4.06–4.07 Ga [*Frey*, 2008; *Robbins et al*, 2013]). The large-scale morphology of the region is characterized by heavily cratered terrain and structures that are likely related to the Hellas impact basin. These structures include concentric scarps and troughs up to ~100 km wide and ~1000 km long that trend NE-SW, or E-W, roughly parallel with the curvature of western Hellas Basin [e.g., *Greeley and Guest*, 1987; *Wichman and Schultz*, 1989; *Tanaka and Leonard*, 1995]. Most of the troughs were previously mapped as “Hellas concentric canyons” by *Wichman and Schultz* [1989] and were interpreted to have formed relatively early in the Hellas tectonic sequence, possibly during collapse of the transient cavity. They suggest that the canyons may be analogous to the Valhalla canyon system on Callisto, where a leading hypothesis for canyon formation is flow of asthenosphere towards the impact center, which creates drag on the base of the lithosphere and leads to surface faulting [*McKinnon and Melosh*, 1980].

[7] In a global compositional classification of surface units using Thermal Emission Spectrometer (TES) data, most of the study region was classified as “group 3” by *Rogers and Christensen* [2007], which is characterized by relatively low feldspar abundance and relatively high olivine and low-Ca pyroxene abundance and is typical of Noachian-aged terrains on Mars. That study, carried out at a spatial resolution of 1 pixel per degree (ppd), focused on large-scale global trends in composition and did not account for small-scale spatial heterogeneity that may be present within the broadly defined regions. Early global mineral mapping using OMEGA data [e.g., *Poulet et al*., 2007] did not contain sufficient data coverage over this particular region for detailed analyses. Higher resolution data sets and increased spatial coverage have allowed for increasingly smaller scale compositional and thermophysical analyses in this region [*Rogers et al*., 2009; *Ody et al*., 2012a, 2012b].

[8] The study region contains surfaces that exhibit an uncommon amount of partially exposed rock compared to much of the Martian surface [e.g., *Edwards et al*., 2009; *Rogers et al*., 2009]. The geologic settings of these surfaces (referred to as “rocky units” in previous work) include crater floors, intercrater plains, and the floors of the Hellas circumferential graben described above. Some of these surfaces were examined with spectral data by *Rogers et al*. [2009], as described in section 1. This work expands the work of *Rogers et al*. [2009] by identifying additional rocky units and characterizing their properties. The *Rogers et al*. [2009] study primarily focused on the differences between the rocky units and surrounding low thermal inertia surfaces. This study primarily focuses on spectral variability within and between rocky units, as well as the broader geologic context and possible origin of those units.

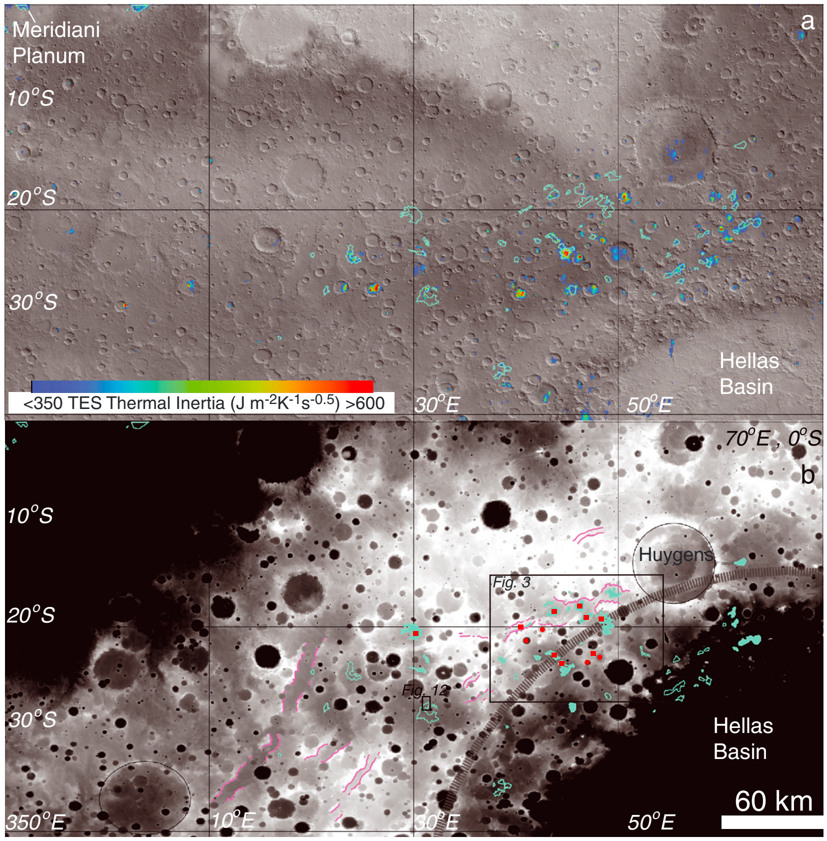

Figure 2. Thermal and topographic characteristics of the study area (350°E–70°E, 0°S–40°S) (a) TES-derived thermal inertia [*Mellon et al.*, 2000] overlain on TES albedo and MOLA shaded relief. Thermal inertia values below 350 $\mathrm{J\,m^{-2}\,K^{-1}\,s^{-0.5}}$ are masked out. Cyan polygons indicate regions of thermal inertia $>350\,\mathrm{J\,m^{-2}\,K^{-1}\,s^{-0.5}}$ that are not associated with crater floors. These include intercrater plains and large graben floors. Large graben are delineated in purple. The THEMIS daytime and nighttime IR radiance mosaics were used to define the polygon boundaries. (b) Noncrater high-TI locations overlain on MOLA elevation (500–2800 m). The thick dashed line indicates the approximate location of the main Hellas basin scarp [*Wichman and Schultz*, 1989]. Filled polygons exhibit a basaltic spectral shape in THEMIS and/or TES data. Nonfilled polygons generally do not have a basaltic spectral shape (see text). Red squares indicate locations where both lithologies (discussed in text) are observed in THEMIS or HiRISE images; red circles indicate locations where both lithologies are observed on crater floors. Locations examined include all noncrater rocky units and some crater floor units. Black polygons show the locations of Figures 3 and 12.

3. Methods

3.1. Thermal Inertia

[9] Thermal inertia (TI) is a property of a surface that describes its resistance to changes in temperature throughout the day [e.g., *Kieffer et al.*, 1999]. It is dependent primarily on bulk thermal conductivity but also the bulk density and specific heat of the material. Surfaces with high bulk thermal conductivity, such as rocks or ice, exhibit high TI values (e.g., $>1200\,\mathrm{J\,m^{-2}\,K^{-1}\,s^{-0.5}}$) [e.g., *Mellon et al.*, 2000; *Fergason et al.*, 2006]. Surfaces with low bulk thermal conductivity, such as dust-covered areas, exhibit low TI values (e.g., $<100\,\mathrm{J\,m^{-2}\,K^{-1}\,s^{-0.5}}$). Intermediate TI values are somewhat difficult to interpret because of the nonunique combination of materials that can give rise to those values, such as indurated soils or unconsolidated, dune-forming sands, or mixtures of rocks and sands [e.g., *Fergason et al.*, 2006]. At the resolution of the TES instrument, much of the Martian surface exhibits TI values $<\sim 350\,\mathrm{J\,m^{-2}\,K^{-1}\,s^{-0.5}}$ [*Mellon et al.*, 2000]. Surfaces with partially exposed rock at the sub-TES pixel scale are commonly found within regions exhibiting TI values greater than 350 $\mathrm{J\,m^{-2}\,K^{-1}\,s^{-0.5}}$ [*Edwards et al.*, 2009].

[10] Because TI estimates are not available on a pixel-by-pixel basis for THEMIS images, we used a combination of TES-derived TI values and qualitative examination of THEMIS daytime and nighttime radiance mosaics [*Edwards et al.*, 2011] to estimate the westward extent of high-TI plains and graben floor surfaces within the study region. TES TI values [*Mellon et al.*, 2000] above 350 $\mathrm{J\,m^{-2}\,K^{-1}\,s^{-0.5}}$ were used to first locate potential rocky surfaces in Java Mission-planning and Analysis for Remote Sensing (JMARS) (http://jmars.mars.asu.edu), a java-based geographic information system (GIS) that accesses global Martian data sets stored at Arizona State University [*Christensen et al.*, 2009] (Figure 2a). The THEMIS mosaics were then used to define the extent of each rocky exposure.

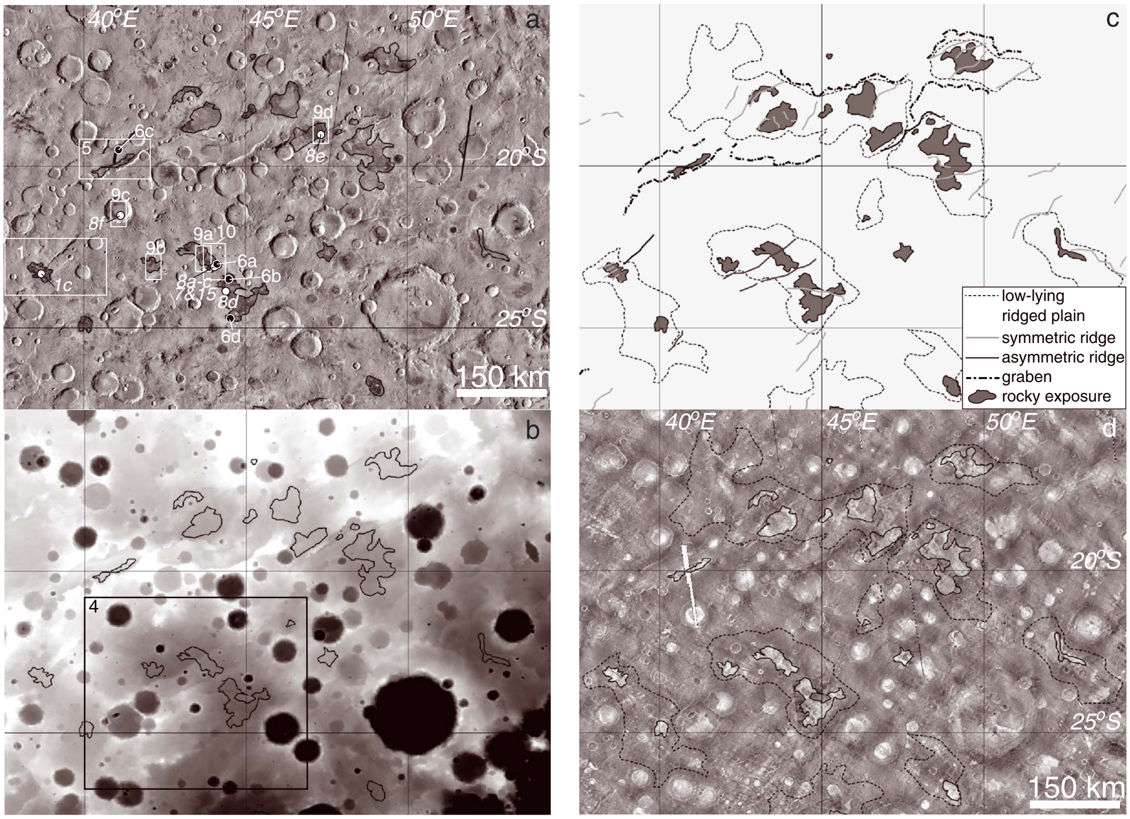

Figure 3. Higher resolution view of rocky units and surroundings in THEMIS and MOLA data. (a) THEMIS daytime radiance mosaic. Noncrater rocky units (delineated using TES thermal inertia and THEMIS day/night IR mosaics) are outlined. Locations of HiRISE (Figures 1 and 8) are indicated with white circles and italicized labels. Locations of CTX images (Figure 6) are indicated with black circles. Locations of THEMIS images (Figures 1, 5, 9, and 10) are indicated with white rectangles. Locations of Figures 7 and 15 approximately coincide with the location of Figures 8a–8c (white circle). (b) MOLA elevations, from 500–2800 m. Note that rocky units are generally found in relatively low plains. Ridges, faults, and grabens are also observed throughout the region. Location of Figure 4 shown with black rectangle. (c) Map of structures observed in MOLA data. Dashed lines: extent of low-lying, ridged plains. Gray lines: ridges, symmetric about the axis. Black lines: asymmetric ridges, likely faults. See also Figure 4. Dash-dotted lines: graben (some of these were mapped as "Hellas concentric canyons" by *Wichman and Schultz* [1989]). (d) THEMIS nighttime IR mosaic, with general locations of low-lying plains and rocky units delineated. Note that the low-lying plains contain rocky units that are commonly partially buried by lower thermal inertia crater ejecta and other sediment.

[11] Maximum TI values were estimated for some of the units from select THEMIS nighttime images using a thermal model (KRC), *Kieffer* [2013], and modified by *Fergason et al*. [2006]. TES climatological data binned at 2° per pixel and 30° heliocentric longitude were queried for the latitude of the surface of interest and the heliocentric longitude at the time of THEMIS image acquisition to retrieve an estimate of visible dust opacity for that image. This dust opacity value, along with latitude, heliocentric longitude average Mars Orbiter Laser Altimeter (MOLA) elevation, average TES albedo, and local time associated with each THEMIS image were used to model surface temperature for a range of TI values. THEMIS surface temperatures (defined as band 9 brightness temperature for nighttime images) of areas of interest were compared with model-derived temperatures to estimate a TI for that surface.

3.2. Spectral Analysis

[12] High spatial resolution spectral analyses were carried out with Mars Odyssey THEMIS [*Christensen et al*., 2004] and Mars Reconnaissance Orbiter CRISM (Compact Reconnaissance Imaging Spectrometer for Mars) [*Murchie et al*., 2007] images. The THEMIS multispectral imager measures infrared radiance in nine channels between ~6.5 and 15 μm at a nominal spatial resolution of 100 m/pixel. THEMIS radiance images were corrected for instrument artifacts and atmospheric influences using the methods described in *Bandfield et al*. [2004]. These corrections were carried out using the THMPROC webtool (http://themis.asu.edu/software) and Davinci image analysis freeware (http://davinci.asu.edu). To identify spectral variability within the rocky units, THEMIS daytime multispectral radiance and emissivity images were decorrelation stretched (DCS) [*Gillespie*, 1992] using bands 8-7-5 displayed as red-green-blue

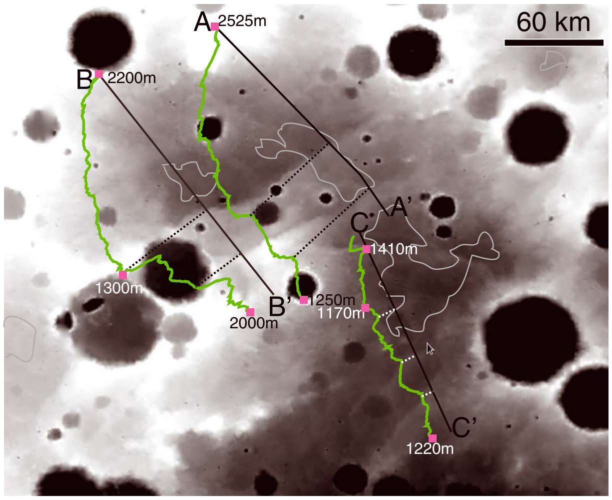

Figure 4. Closer view of ridge topography from MOLA (see Figure 3b for figure location). Thin gray lines indicate locations of rocky exposures. Dashed lines indicate ridge locations on the transect lines. A-A′ and B-B′ transect ridges that are asymmetric about the ridge axis. One side of the ridge is higher than the other by ~200–400 m. These ridges continue into the adjacent higher terrains and are likely faults. C-C′ transects lower relief ridges (~50–100 m) that are generally confined to the low-lying plains and are roughly symmetric about the axis.

(RGB). Other band combinations were also examined, but bands 8-7-5 best captured the spectral variability in the images. Spectral differences identified in the DCS images were quantified by extracting and comparing average surface emissivity spectra from each unit.

[13] The CRISM instrument acquires reflected solar energy between ~0.36 and ~3.9 μm in 544 channels and has a maximum spatial resolution of ~18 m/pixel. For this work, we excluded wavelengths below ~0.7 μm because of atmospheric scattering effects and also excluded the ~2.6–3.9 μm spectral region because of radiative influence from thermal emission which requires additional thermal correction. Though using only the ~0.7–2.6 μm range means less information for our study, this range still captures most of the crystal field absorptions and vibrational overtone/combination frequencies associated with Fe-, OH-, H_2O-, and CO_3-bearing minerals. CRISM "*I/F*" images (where I = surface radiance and F is solar irradiance at the top of the atmosphere) were corrected for atmospheric gas contributions by scaling a typical Martian atmospheric spectrum to match the depth of gas bands in the measured spectrum and then ratioing the measured spectrum by the scaled atmospheric spectrum [*McGuire et al.*, 2009]. These preprocessing steps were carried out using the CRISM Analysis Toolkit (http://pds-geosciences.wustl.edu/missions/mro/crism.htm) developed for ENVI software. Spectral indices (also known as "summary parameters") similar to those derived by *Pelkey et al.* [2007] were generated for each image examined. The index formulations are designed to highlight the presence and relative concentration of certain mineral groups. Areas highlighted by the indices were examined in detail by first creating polygons of ~50–550 pixels over regions of interest in the map-projected image and then extracting average corrected *I/F* spectra from those polygons. These average spectra were then ratioed to nearby neutral surfaces to enhance the spectral features of the material of interest. For THEMIS-derived spectral units that were large enough to be isolated in Mars Global Surveyor TES data (~3 × 8 km field of view for each detector), TES spectra were extracted and analyzed. With 143 channels and a wider spectral range (~6–50 μm), the TES instrument provides complementary spectral information to the THEMIS multiband imager. TES data are corrected for atmospheric contributions by finding the best fit to the measured spectrum using a library of mineral and atmospheric component (dust, water ice, CO_2, water vapor) spectra [e.g., *Bandfield*, 2002]. The atmospheric component spectra are then scaled by their modeled abundance and subtracted from the measured spectra to yield surface emittance. The linear least squares minimization routine [*Bandfield*, 2002; *Rogers and Aharonson*, 2008] that is used to determine the atmospheric contributions also yields estimates of

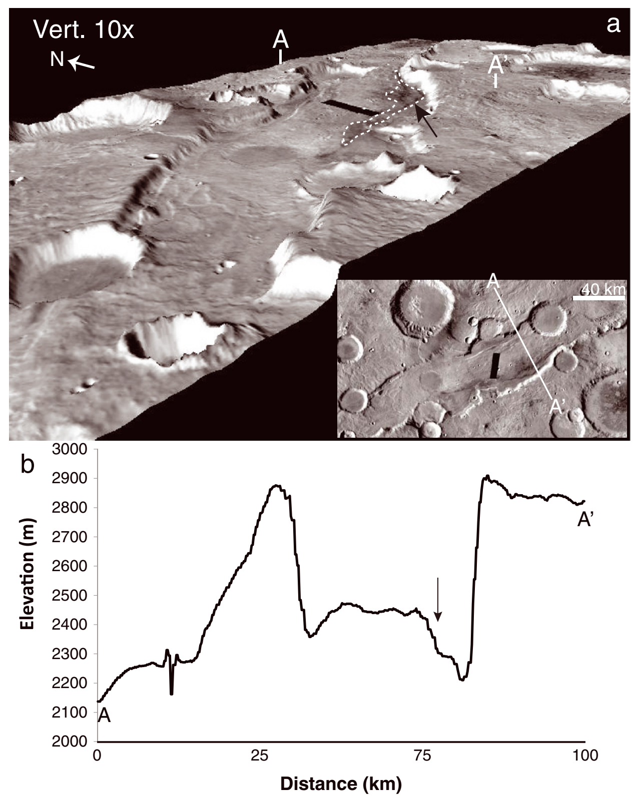

Figure 5. Raised graben fill near 41°E, 19.5°S (see location in Figure 3a). Younger units within the graben have a rounded topographic profile and do not meet the graben walls. Parts of the fill unit profile have a staircase appearance, suggesting vertical variation in erodability/structural competence (black arrows in Figures 5a and 5b). (a) THEMIS daytime IR draped over MOLA 128 ppd gridded product. Vertical exaggeration is 10×, and the view is towards the NE. Inset shows 2-D view of the area and transect location shown in Figure 5b. Dashed lines indicate areas with rocky exposures. (b) MOLA gridded elevation from A-A′, as shown in Figure 5a. Vertical exaggeration is 35×.

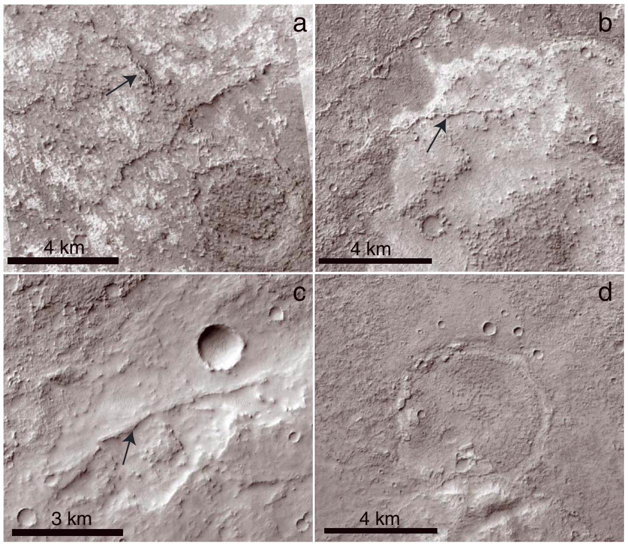

Figure 6. Morphologic features observed in CTX data. Figures 6a–6c are examples of raised, linear features that may be dikes. Figure 6d is a ~5 km diameter ghost crater within the rocky unit. (a) Portion of CTX image P16_007254_1586_XN_21S316W centered at 23.0°S, 44.0°E. (b) Portion of CTX image B20_017262_1550_XI_25S315W centered at 23.6°S, 44.4°E. (c) Portion of CTX image P21_009113_1598_XN_20S318W centered at 19.5°S, 41.0°E. (d) Portion of CTX image B20_017262_1550_XI_25S315W.

mineral abundance by normalizing the modeled contributions of mineral spectra by the sum of all modeled surface components. For this study, we used the spectral library of *Rogers and Fergason* [2011].

3.3. Analysis of Structure and Morphology

[14] Gridded elevation data (128 ppd) derived from the Mars Global Surveyor Mars Orbiter Laser Altimeter (MOLA) [*Smith et al.*, 1999] were used to locate large-scale structural features in the region, such as ridges, faults, troughs, massifs, and low-lying plains. High-resolution images from the MRO High Resolution Imaging Science Experiment (HiRISE) [*McEwen et al.*, 2007] camera and Context Imager (CTX) [*Malin et al.*, 2007] were used to characterize the morphology and stratigraphic relations between spectral units identified with THEMIS. HiRISE images shown in this paper have spatial resolutions between 25 and 50 cm/pixel; CTX image resolution is ~6 m/pixel. To characterize small-scale stratigraphic relationships, a digital elevation model (DEM) was generated from an overlapping pair of map-projected CTX images using the NASA Ames Stereo Pipeline v2.0 automated stereogrammetry software [*Broxton and Edwards*, 2008; *Moratto et al.*, 2010].

3.4. Crater Retention Age Estimates

[15] Crater retention ages were calculated to estimate emplacement ages of the rocky units in two different ways. The two different crater counting methods were used to evaluate

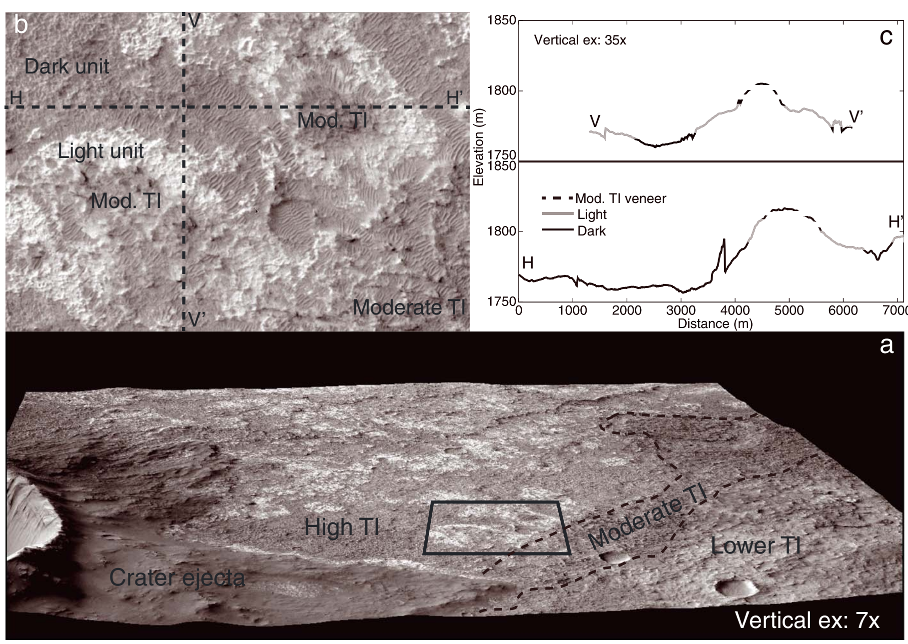

Figure 7. (a) CTX image draped over CTX DEM generated from stereo pairs P16_007254_1586_XN_21S316W and P17_007610_1572_XN_22S316W. Image center is approximately 23.19°S, 43.95°E which generally coincides with Figure 8a; location can be observed in Figure 15b. Contacts between the high-TI plains, moderate-TI veneer, and low-TI mantled plains are illustrated with dashed lines. Polygon shows location of Figure 7b. View is toward NNW. (b) CTX zoom showing the dark and light-toned units and the moderate-TI veneer. Dashed lines show locations of profiles in Figure 7c. (c) Topographic profiles of H-H′ and V-V′, colorized to show locations of the dark-toned and light-toned units, as well as the veneer unit. From these profiles, and others within this scene (not shown), we estimate a maximum thickness of ~30 m for the light-toned unit.

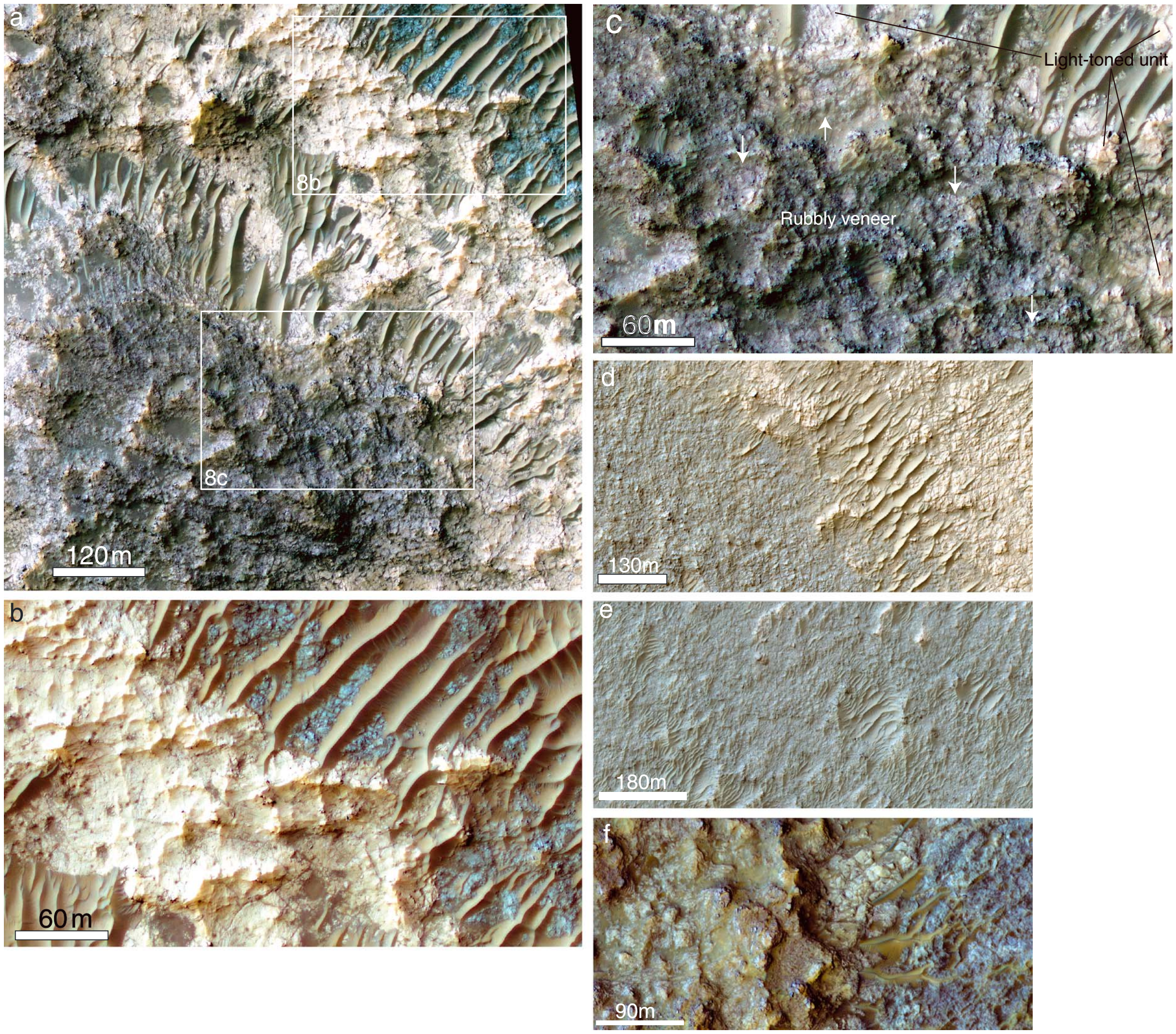

Figure 8. High-resolution views of rocky exposures (locations shown in Figure 3a). At least two units are observed. The images show a light-toned unit overlying a dark-toned unit; these units exhibit an absolute reflectance difference of ~0.05, between ~1.0 and 2.5 μm (section 4.2). Aeolian bed forms are also observed. (a) Portion of HiRISE image PSP_007254_1565_COLOR.JP2 (25 cm/pixel) showing the dark-toned unit, light-toned unit, and rubbly veneer. Locations of Figures 8b and 8c are indicated with white polygons. (b) Portion of HiRISE image PSP_007254_1565_COLOR.JP2 (25 cm/pixel) showing light-toned unit overlying dark-toned unit. (c) Portion of HiRISE image PSP_007254_1565_COLOR.JP2 (25 cm/pixel) showing a thin layer of dark-toned boulders and sediment overlying the light-toned unit. White arrows point to regions where the characteristic polygonal fracturing of the light-toned unit can be observed through the dark veneer. (d) Portion of HiRISE image ESP_017262_1560_COLOR.JP2 (50 cm/pixel) showing polygonally fractured light-toned unit overlying dark-toned unit. (e) Portion of HiRISE image ESP_017697_1605_COLOR (50 cm/pixel), showing dark-toned unit overlain by isolated lighter bed forms, and isolated remnants of the light-toned unit. (f) Portion of ESP_013504_1580_COLOR.JP2, (25 cm/pixel) showing polygonal forms and variability within the light-toned unit on a crater floor.

the differences in model age when smaller areas and craters are used instead of larger areas and craters. Surface age estimates of contiguous high thermal inertia areas (gray-shaded polygons in Figure 3c) were carried out using the methods of *Michael and Neukum* [2010]. Counting was done on the highest quality THEMIS VIS images (18 m/pixel resolution) [*Christensen et al*., 2004] devoid of stray light artifacts. Projected THEMIS VIS images were loaded into ArcGIS, and crater counting was done using the Free University of Berlin's ArcGIS toolbar, CraterTools [*Kneissl et al*., 2011]. Craters with a diameter greater than 250 m were counted. Craters and counting areas that clearly appeared in clusters or chains were excluded to negate the influence of secondary cratering. Counts were then double checked for completeness. Craters were run through Craterstats' randomness and spatial analysis tool [*Michael et al*., 2012], and outputs were examined to further ensure that secondary cratering did not influence the counts. Fitting ranges were chosen based on the best fits through the largest diameter population of craters before clear evidence

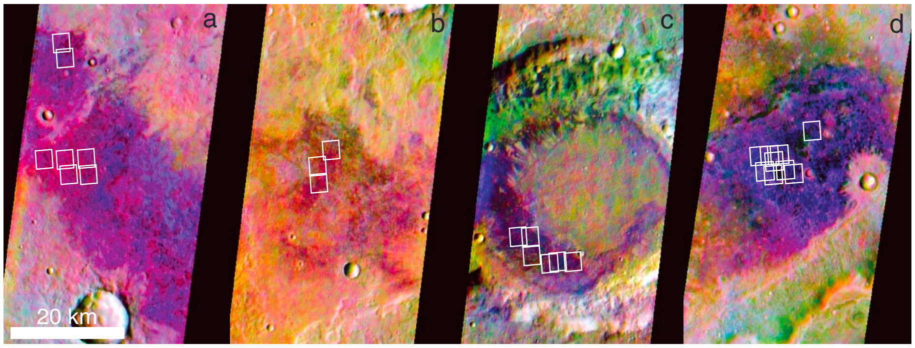

Figure 9. Examples of THEMIS spectral variability observed within each rocky unit. Locations of TES spectra used to derive unit averages in Figure 13 are overlain on THEMIS DCS radiance images, using bands 8-7-5 as red, green, and blue. Rocky units appear magenta or purple in these stretched images. The first three panels show locations of spectral extractions from the upper, light-toned unit. The last panel shows locations of spectral extractions from the lower, dark-toned unit. From left to right, the image IDs are: I08288002, I09611002, I09948002, and I42118002.

for resurfacing or resolution runoff (indicated by a dropoff in slope below the fitted isochron).

[16] The counting areas and the crater populations within this unit were relatively small for such an old terrain, so the craters used in fitting ranges may have been influenced by resurfacing. To test this, we investigated the differences in estimated ages when counting areas were expanded to include areas within the same unit that are covered with a veneer of mantling material (dashed polygons in Figure 3c). For the low-lying ridged plains mapped in Figure 3c, we counted crater frequency as a function of diameter for all craters above 1 km diameter from the *Robbins and Hynek* [2013] crater database. In general, the exposed rocky portions of the low-lying ridged plains contained only three or four craters per counting area within the fitting ranges unaffected by resurfacing (3–40 km in diameter). ArcGIS shapefiles containing the database were acquired from the U.S. Geological Survey Planetary GIS Web Server. All craters with centers lying within the outcrop were selected for age estimation. Craters were examined individually for accuracy, and any areas with obvious clusters or chains of craters were eliminated to negate the influence of secondary cratering. Cumulative size-frequency diagrams (CSFD) were created in Free University of Berlin's Craterstats II software (http://hrscview.fu-berlin.de/craterstats.html), and isochrons were fit to CSFDs to estimate ages and uncertainties using the production function of both *Ivanov* [2001] and *Hartmann* [2005] and the chronology function of *Hartmann and Neukum* [2001].

4. Results

4.1. Distribution and Morphologic Characteristics of High-TI Surfaces

[17] High-TI surfaces are primarily concentrated on the eastern side of the study area (Figure 2). Though the majority of the high-TI regions are associated with crater floors, a few are associated with intercrater plains surfaces or the floors of large, fault-bounded troughs (Figure 2a). Maximum TI values derived from THEMIS data for each high-TI exposure range from 360 to $<1200\,\mathrm{J\,m^{-2}\,K^{-1}\,s^{-0.5}}$, with a median and average maximum TI value of 570 and $620\,\mathrm{J\,m^{-2}\,K^{-1}\,s^{-0.5}}$, respectively. Maximum TI values were derived for a few of the flat-floored craters; these range from 480 to $720\,\mathrm{J\,m^{-2}\,K^{-1}\,s^{-0.5}}$. In high-resolution imagery (described below), isolated bed forms are commonly observed overlying polygonally fractured bedrock, consistent with these high TI values. Some of the rocky units on the plains have a circular form, suggesting that they once formed in small craters whose rims and ejecta have been completely removed and indicating their resistance to erosion. Except for exposures in crater floors, there are no occurrences of rocky units on regionally high-standing areas (Figure 3).

[18] Though the crater-hosted high-TI units are more common, this study focuses primarily on the intercrater plains and trough units for several reasons. First, rocky material found contained within a crater could have a variety of origins [e.g., *McDowell and Hamilton*, 2007; *Edwards et al.*, 2009; *Mest and Crown*, 2005; *Rogers and Fergason*, 2011] that likely varies from one crater to the next. Detailed analysis of each crater is beyond the scope of this study. Second, high-TI crater floors are found throughout the cratered highlands of Mars, while intercrater plains high-TI units are mostly confined to a few areas [*Edwards et al.*, 2009, 2010], possibly indicating something unique about these locations. Third, a global, detailed study of high-TI crater floors is forthcoming by Edwards et al. (Impact induced decompression melting of the Martian mantle: The formation of widespread infilled craters and intercrater plains, under review), with preliminary results described in *Edwards et al.* [2013]. We do include some observations of crater-hosted bedrock, where they have similar characteristics to plains units and where interpreted to have a common origin as the plains units.

[19] The rocky units have undergone extensive degradation and partial to complete burial by impact ejecta and sediments. Many of the exposures are partially buried by impact ejecta and thin layers of sediment, which can be readily observed in THEMIS nighttime radiance images [*Rogers et al.*, 2009] (Figure 3d). Obscuration by sediment makes the true extent of these units, as well as the nature of the contact between the high-TI units and the low-TI plains, difficult to discern. However, because the rocky units tend to only be found in topographic lows and not on higher standing ridges or massifs (Figure 3b), we assume that these units may

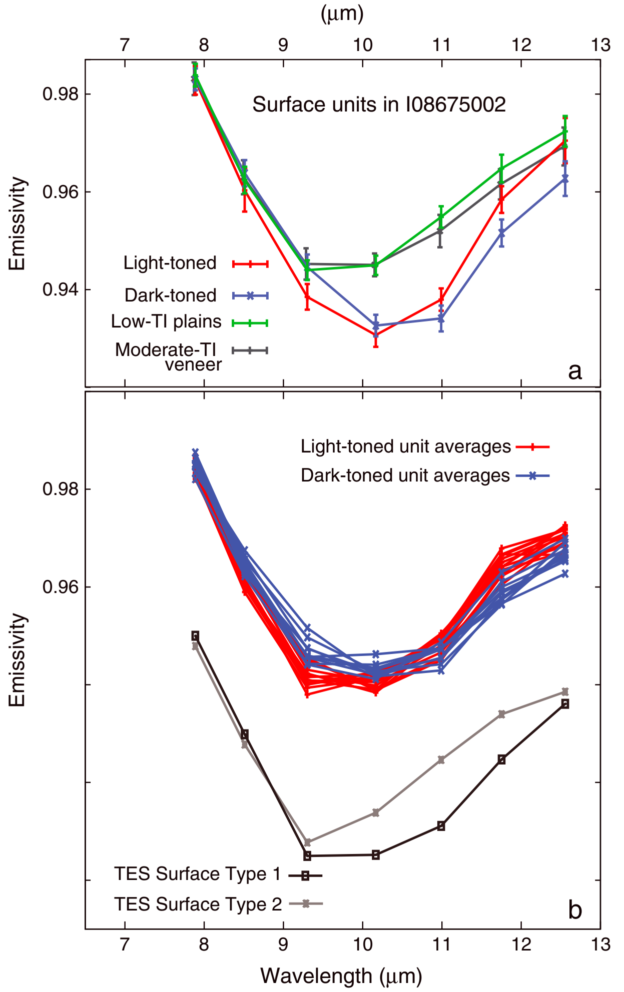

Figure 10. (a) Average surface emissivity from select locations within the light-toned unit dark-toned unit, low-TI plains, and moderate-TI unit in THEMIS image I08675002. Standard deviations on the averages are represented by vertical bars. This region is one of two where the stratigraphic relationship between the light-toned and dark-toned units is best preserved and the units are well isolated from each other at THEMIS spatial resolution. In most other high-TI regions in this study, subpixel mixing makes it difficult to truly isolate the spectral character of each unit, and averages from each unit do not separate by more than a standard deviation. The low-TI and moderate-TI veneer units are not statistically separable from one another. (b) Average THEMIS surface emissivity from the light-toned and dark-toned units from other THEMIS images. Variability within each group is attributed to either real surface variability and/or imperfect surface emissivity derivation during the removal of atmospheric components. TES-derived global surface emissivity end-members [*Bandfield et al*., 2000], degraded to THEMIS resolution, are shown for comparison.

comprise all of the low-lying plains and use MOLA data to place an upper limit on the outward extent of each unit (Figure 3c).

[20] Large-scale ridges are observed on nearly all rocky units (Figures 3c and 4). Some of these ridges are curvilinear, roughly symmetric about the ridge axis, ~3–5 km wide, and confined to low-lying regions of the study area (Figures 3b and 3c). We interpret these as wrinkle ridges, similar to those found in the Hesperian ridged plains and previously attributed to contraction associated with thin-skinned tectonics [*Plescia and Golombek*, 1986]. Other large-scale ridges are linear, asymmetric about the ridge axis, and vertically offset not only the rocky units but also the adjacent, degraded plains and massif units (Figures 3b, 3c, and 4). Because these appear to result in substantial vertical offset (~200–400 m) of both the low-lying plains and the adjacent high-standing areas (Figure 4), we interpret these asymmetric ridges as faults.

[21] Rocky units found on the floors of some of the fault-bounded troughs are associated with a rounded, raised plateau that, at THEMIS IR resolution, appears smoother and less cratered than surrounding plains cut by the trough (Figure 5a). A transect across the graben walls and floor show that the graben fill has a rounded topographic profile and does not meet the graben walls. Parts of the fill unit profile have a "staircase" appearance, suggesting vertical variation in structural competence of the material (Figure 5b).

[22] Small-scale morphologic features observed in the rocky units include heavily degraded ridges, infilled craters, and variations in tone/texture (Figure 6). The textural/tonal variations correspond to different lithologies and are described in more detail in section 4.2. The infilled craters are similar to "ghost" craters found in mare on the Moon and Mercury, which have been interpreted as volcanically infilled craters [e.g., *Cruikshank et al*., 1973; *Klimczak et al*., 2012]. Small, raised linear features of 50 to 100 m width are also found within the exposures (Figure 6). Their origin is unclear, but they may be exposed dikes. Compared to other dikes which were mapped to the northeast of our study region by *Head et al*. [2006], these features are much narrower (~100 m versus ~1 km), more sinuous, and exposed over much shorter distances (~a few km versus tens of km). There is a lack of evidence for fine-scale layering or volcanic flow fronts within the rocky units. As described above, the rocky units are heavily degraded; thus, evidence of original morphologies may be obscured or removed.

[23] The total bedrock unit thickness, while variable, is estimated not to exceed ~200 m. This estimate is based on the spectral properties of crater ejecta from craters that occur within the bedrock units. Ejecta from smaller craters appear spectrally similar to the bedrock unit; ejecta from larger craters appear spectrally similar to the surrounding low-TI plains [*Rogers et al*., 2009]. We interpret this to indicate that the larger craters are excavating older, compositionally distinct units that lie below these rock units and use the crater diameter of the smallest spectrally distinct crater and the excavation depth to diameter ratio of (~0.1) [e.g., *French*, 1998] to estimate the thickness. This ~200 m thickness is consistent with the top-to-bottom elevation difference of the graben fill material shown in Figure 5.

4.2. At Least Two Mafic Units Found in Stratigraphy

[24] HiRISE and CTX images reveal that at least two lithologies (a dark-toned and light-toned unit) are present within some of the rocky exposures; these lithologies vary in texture and tone (Figures 7 and 8). Figure 7 shows a

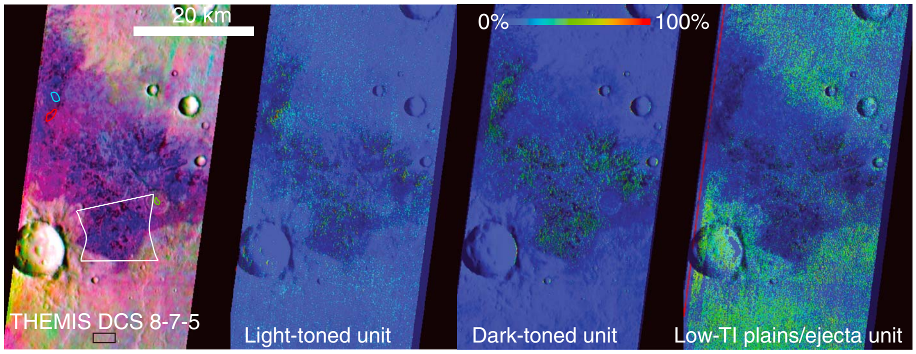

Figure 11. THEMIS view of the type locality for the stratigraphy described in section 4.2. The left panel shows a DCS image (THEMIS I08675002) using bands 8-7-5 as red-green-blue. Red and blue polygons show locations where spectra were extracted from the light-toned and dark-toned unit, respectively. Black polygon shows where spectra were extracted from the low-TI plains, and green polygon shows where spectra were extracted from the moderate-TI veneer material (see text). Spectra shown in Figure 11. The next three panels show the distributions of each unit in the scene, modeled using the spectra from Figure 9. Color bar (0–100%) applies to all three panels. Location of Figure 15 also shown on the left-most panel.

high-resolution view of the stratigraphy present within the high-TI units and surrounding plains. The stratigraphically lowest high-TI unit is dark toned. This dark-toned unit is overlain in some areas by a light-toned unit that is no more than ~30 m thick. No evidence of an embayment relationship is observed between the dark- and light-toned units; thus, we interpret the discontinuous nature of the light-toned unit to indicate that they are isolated erosional remnants of a once more extensive unit. At the resolution of HiRISE, polygonal fractures are commonly observed within both the dark-toned and light-toned units (Figure 8). The light-toned unit also commonly contains dark-toned lineaments that crisscross the unit (orientations were not measured). Of the 17 HiRISE images that were examined, no evidence for fine-scale layering was observed within the high-TI units in the intercrater plains or troughs. This stratigraphy is well preserved in only a few locations. In many locations, only small erosional remnants of the light-toned unit can be observed (e.g., Figures 1 and 8e); in some cases, the presence of bed forms makes it difficult to discern the extent of both units.

[25] A third unit, which is dark toned and contains an abundance of boulders (<2 m) and sediment compared to the lower two units (Figures 8a and 8c), is also observed in some places. This unit also exhibits a lower TI than the dark- and light-toned units described above (~410 $J\,m^{-2}\,K^{-1}\,s^{-0.5}$ in THEMIS image I05323005, versus ~650–950 $J\,m^{-2}\,K^{-1}\,s^{-0.5}$ for the dark- and light-toned units). In some instances, this moderate-TI third unit is overlying the light-toned unit. In

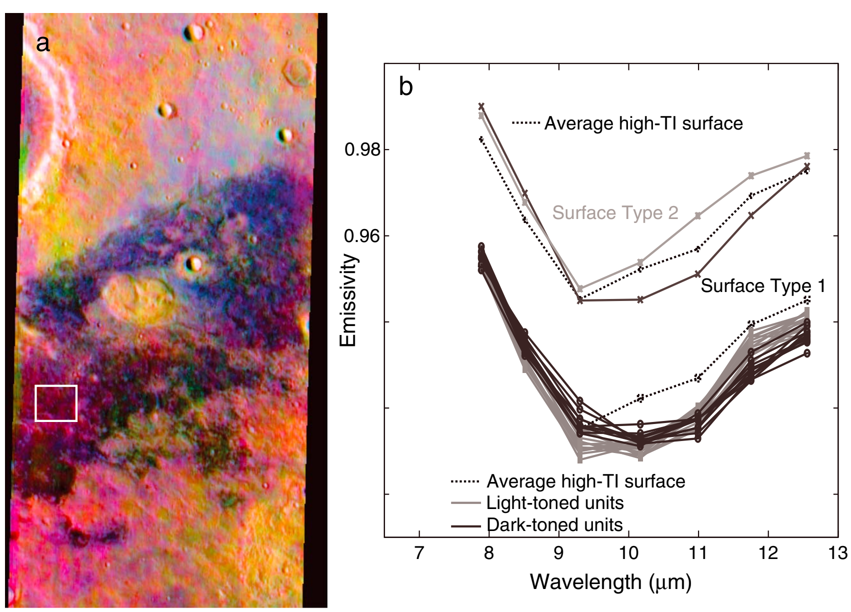

Figure 12. (a) THEMIS DCS image I08226002 over rocky exposure near 31.1°E, −27.8°S. (b) Average surface emissivity from highest-TI location within the exposure shown with white polygon in Figure 12a, compared with average surface emissivity from other high-TI exposures and also with TES Surface Types 1 and 2. Not all rocky exposures in the study region exhibit the spectral properties shown in Figures 10, 11, and 13.

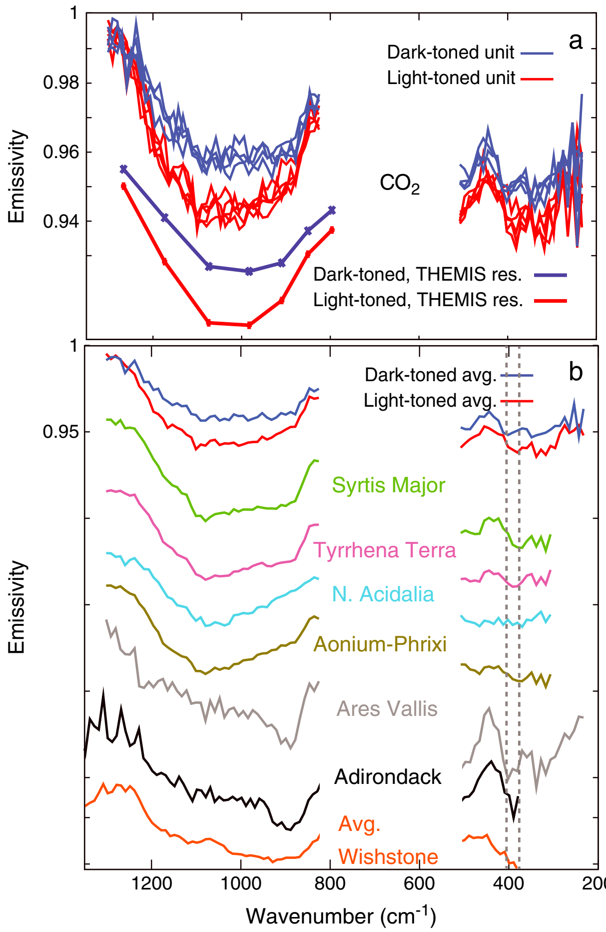

Figure 13. (a) Derived surface emissivity spectra from the light and dark-toned units observed in THEMIS images. Each spectrum represents the derived surface emissivity from a single orbit that crosses the unit of interest and has been normalized to the average spectral contrast observed within each group. These spectra were averaged and convolved to the THEMIS bandpasses to show how the surface units should appear at THEMIS spectral resolution. (b) The average surface emissivity spectrum from each unit compared with other TES-derived global/local-scale units and Mini-TES spectra of select rocks at Gusev crater. The Syrtis Major, Tyrrhena Terra, Acidalia Planitia, and Aonium Planum spectra are from *Rogers and Christensen* [2007]. The Ares Vallis spectrum is from *Rogers et al.* [2005]. The Adirondack spectrum is the dust-corrected Adirondack spectrum from sol 11, from Figure 8b of *Hamilton and Ruff* [2012]. The Wishstone spectrum is the average Wishstone class Mini-TES spectrum from Figure 20 of *Ruff et al.* [2006]. Vertical dashed lines are intended to help the viewer compare absorptions between units.

others, it appears to be in direct contact with the lower dark-toned unit (Figure 7). At HiRISE resolution, the polygonal texture of the light-toned unit can be observed through this third unit (Figure 8c), suggesting that the third unit is only a thin veneer of sand and rubbly material. As described below, this third unit is olivine-poor and spectrally indistinguishable from the low-TI plains. Based on the spectral similarity between this unit and the surrounding low-TI mantling material, as well as the lower TI and lack of clear outcrop, we

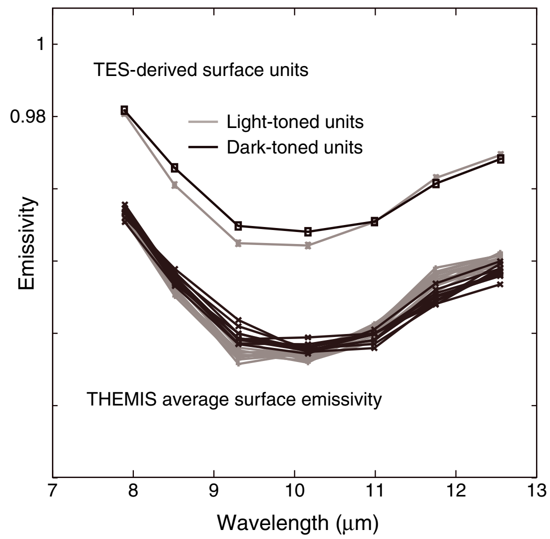

Figure 14. Comparison of TES-derived spectra from each bedrock unit, with THEMIS surface emissivity spectra from each unit. TES-derived spectra are from Figure 13a, convolved to THEMIS resolution and scaled to the average spectral contrast. THEMIS surface spectra are from Figure 11b.

interpret this material to be a thin veneer unit that was deposited unconformably over the other two units, loosely lithified, and has since been removed in many places via erosion. Based on spectral similarity with the lower TI plains, these plains may have been the source of the veneer material.

[26] The two high-TI units observed in HiRISE images (Figure 8) exhibit spectral differences in THEMIS images (Figures 7–9). The possibility of multiple spectral units in the bedrock was noted by *Rogers et al.* [2009]; however, the dearth of supporting high-resolution imagery prohibited detailed analysis at the time of that study. In general, the lower, dark-toned unit appears blue in the THEMIS DCS 8-7-5 images, and the upper, light-toned unit appears red. However, for rocky exposures where only one of the units is present, the units (either dark toned or light toned) can appear either blue or magenta in THEMIS DCS 8-7-5 images. This is because the decorrelation stretch uses scene statistics to find the principal axes of spectral variability and generate the stretch; if only one unit is present, it affects the statistics differently than if there are two or more units present. This hinders straightforward identification of each unit in the THEMIS DCS images. To identify the presence of each unit, surface emissivity spectra must be derived and examined. Another challenge in identifying which unit is present is the fact that

Table 1. Modeled Compositions (Areal %)

	Dark Toned	Light Toned
Feldspar	33(6)	38(5)
Pyroxene	37(4)[a]	32(4)[b]
Olivine	7(3)	9(3)
High-silica phases	9(6)	10(6)
Sulfate	6(2)	6(2)
Carbonate	5(1)	3(1)
Quartz	1(2)	2(1)
Hematite	2(2)	0

[a]Dominated by high-Ca pyroxene.
[b]Dominated by low-Ca pyroxene.

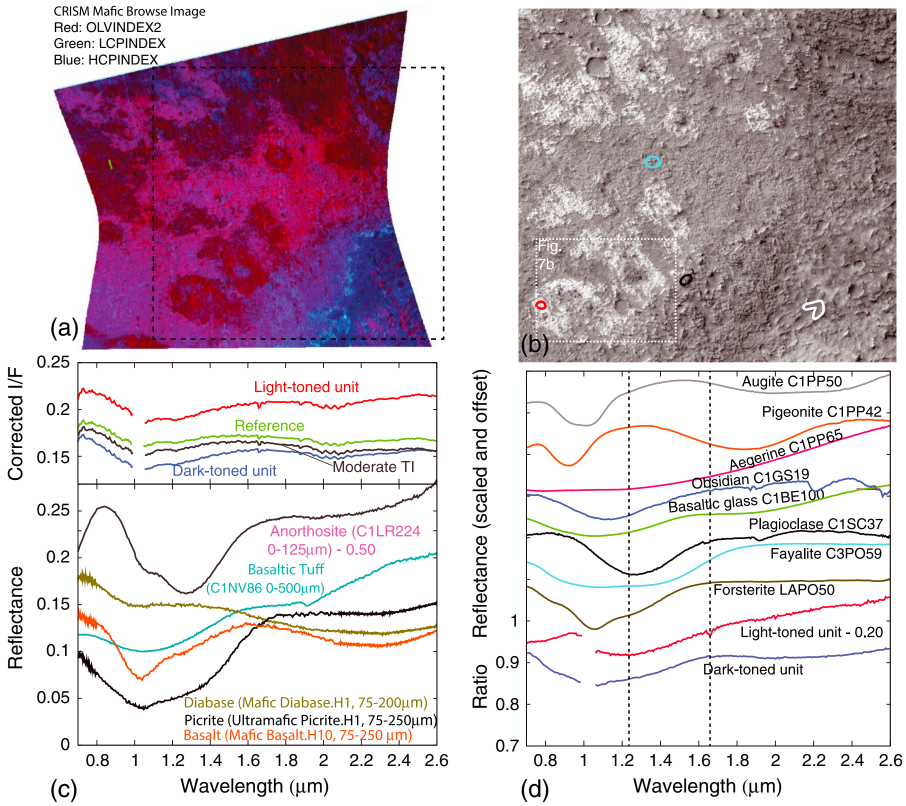

Figure 15. Analysis of CRISM image FRT00009E61; location shown in Figure 10. (a) RGB composite of olivine (OLVINDEX2), low-Ca pyroxene(LCPINDEX), and high-Ca pyroxene (HCPINDEX) summary parameters[*Pelkey et al*., 2007; *Salvatore et al*., 2010]. The summary parameters are stretched using fixed high and low values, which were selected by the CRISM team based on globally determined high and low values for these indices (OLVINDEX2: 0–0.13; LCPINDEX: 0–0.10; HCPINDEX: 0–0.20). Dashed square shows location of CTX image in Figure 15b. The color composite suggests that the light-toned unit is enriched in olivine, and the dark-toned unit is enriched in olivine and HCP. (b) Portion of CTX image P16_007254_1586_XN_21S316W Polygons show locations of CRISM spectral extractions shown in Figure 15c. Dashed white polygon shows location of Figure 7b. (c) CRISM *I*/*F* spectra extracted from the dark and light-toned bedrock units, the moderate-TI veneer, and a "reference" surface for ratioing. As described in the text, no spectrally neutral surfaces are found in this scene. The reference surfaces were chosen from lower TI regions near the margin of the bedrock; they likely represent a mixture of sand and dust. The moderate-TI veneer is nearly identical in shape to the reference surface. The dark-toned and light-toned unit spectral shapes do not differ greatly from each other, but subtle differences can be observed in the ratio spectra (in Figure 15d). The light-toned unit exhibits ~0.05 higher reflectance across most of the wavelength range shown. Laboratory spectra of coarse grained igneous rock particulates from the Brown University RELAB and Johns Hopkins University spectral libraries [*Salisbury et al*., 1991] are shown for comparison. No offsets or scaling were applied to the laboratory or CRISM spectra, except for the anorthosite sample (subtracted 0.5). The units do not resemble the laboratory samples selected for comparison; however, there may be contributions from dust or sediment that obscure the true spectral character. (d) Ratio spectra generated by dividing the dark and light-toned unit spectra by the reference surface in Figure 15c. These spectra are difficult to interpret because they contain information about both the surface of interest and the reference surface, and the shapes are sensitive to the choice of denominator. Nevertheless, we use the ratios to better visualize the subtle differences between the dark and light-toned units and also to verify the lack of absorptions due to H_2O or OH. The light-toned unit ratio contains a broad minimum near ~125 μm (short-wave vertical dashed line), whereas the dark-toned unit ratio has a broad minimum near ~1.1 μm. The dark-toned unit also has a distinct inflection near ~1.65 μm (long-wave vertical dashed line) that is absent from the light-toned unit ratio. The ratio spectrum from the dark-toned unit is consistent with enrichment of olivine relative to the reference surface. The ratio spectrum from the light-toned unit is not consistent with olivine, because of the lack of inflection at ~1.65 μm and the band minimum shifted towards ~1.25 μm. It may be consistent with feldspar (see also *Wray et al*. [2013]) or possibly glass; however, we note that broad band positions are highly sensitive to the slope of the denominator spectrum; thus, it is difficult to confidently interpret the ratio spectra of these units.

Table 2. Locations and Characteristics of Regions Used for Crater Model Ages

Area #	Center Long, Lat	Ivanov PF Age (Ga)	Hartmann PF Age (Ga)	Uncertainty (Ga)	Counting Area (km^2)	# of Craters Fit	Fitting Range (km)
1	31.0E, −28.5	3.92	3.94	+0.03 −0.03	5.61×10^4	27	6–35
2	28.6E, −20.3	3.91	3.93	+0.03 −0.03	5.01×10^4	29	5–40
3	43.7E, −17.9	3.80	3.82	+ 0.04 −0.06	4.59×10^4	11	7–20
4	43.6E, −23.3	3.86	3.83	+0.03 −0.04	2.48×10^4	22	3–20
5	45.0E, −27.5	3.94	3.93	+0.04 −0.06	1.96×10^4	9	7–30
6	48.8E, −20.0	3.95	3.97	+0.04 −0.06	1.92×10^4	8	6–40
7	39.6E, −24.7	3.97	3.98	+0.04 −0.05	1.83×10^4	14	6–25
8	52.7E, −22.8	3.91	3.89	+0.04 −0.07	1.19×10^4	9	4–17
9	49.8E, −16.9	3.87	3.86	+0.06 −0.1	1.02×10^4	5	4.5–25

the surface emissivity differences between the two units are rather subtle at THEMIS spectral resolution. Figure 9 shows derived surface emissivity from multiple rocky unit exposures where both units appeared to be present in either THEMIS or HiRISE data. The lower unit (blue in THEMIS DCS) has a lower emissivity between ~11.0 and 12.5 μm relative to 9–10 μm. However, in general, both units appear basaltic at THEMIS spectral resolution and similar to TES Surface Type 1 (a commonly observed basaltic spectral shape derived by *Bandfield et al*. [2000] using TES data). The last complication is that many of the rocky units are partially covered by bed forms, which results in mixed pixels at THEMIS resolution and hinders straightforward identification of the presence of both units. Using derived THEMIS surface emissivity spectra from multiple images, we determined the locations where each unit is definitely or tentatively present (Figure 2b). Finally, we note that the moderate-TI unit is not statistically distinguishable from the low-TI mantled plains (Figure 10); both appear green in DCS 8-7-5 images (Figure 11).

[27] Not all high-TI units exhibit these spectral properties. Units in the southern portion of the study area tend to exhibit similar textures and morphology but spectrally appear more similar to TES Surface Type 2 (which is dominated by high-silica poorly crystalline or amorphous phases) (Figure 12). It is unclear whether these units represent primary compositions or whether they were similar to more northerly exposures but have been chemically altered. Their higher latitude positions are consistent with increased chemical alteration via frost/ice-driven processes. Other units toward the center of the study region (Figure 2) also appear more similar to Surface Type 2; however, they are at similar latitude to the basaltic exposures to the east. They may represent a different lithology or may be influenced by higher proportion of low-TI regolith. The maximum THEMIS TI values for these exposures are on the low end of the range given in section 4.1 (~475 $J\,m^{-2}\,K^{-1}\,s^{-0.5}$) and do appear to have fewer "warm" pixels in the THEMIS nighttime radiance mosaic, suggesting regolith cover is a likely explanation.

[28] Figures 3 and 9 show locations where each unit is exposed over a large enough area to be isolated in TES data. For the light-toned unit, TES spectra were extracted from three locations and a total of five orbits (Figures 9 and 13). For the lower, dark-toned unit, TES spectra were extracted from one location and a total of four orbits (Figures 9 and 13). A consistent spectral shape is retrieved from each orbit, despite variability in atmospheric contributions between orbits, which substantiates the accuracy of the derived shapes. The average TES-derived shape from each of the two units was degraded to THEMIS resolution (Figure 13a) and compared with the average THEMIS-derived spectral shapes from each unit (Figure 14). The good match between TES and THEMIS suggests that the two units were well isolated in the TES spectra used to derive the average spectrum. (THEMIS surface spectra were derived using different TES orbits than those used to isolate the two units in TES data, providing an independent estimate of surface emissivity between the two data sets.) Derived modal abundances from each average TES spectrum indicate that the light-toned unit is distinguished from the dark-toned unit by (1) a higher feldspar-to-pyroxene ratio and (2) a dominance of the low-Ca variety of pyroxene (modeled high-Ca: low-Ca pyroxene proportions are ~1:5, versus 1.5:1 in the lower unit) (Table 1). Modeled olivine abundance in the bedrock units, though higher than the surrounding low-TI plains, is only between ~7 and 10%. Thus, the units are olivine-rich compared to the surrounding plains but not when compared to other olivine-rich rocks on Mars [e.g., *Hamilton and Christensen*, 2005; *McSween et al*., 2008; *Koeppen and Hamilton*, 2008].

[29] Analysis of one CRISM image over the type locality for this stratigraphy is shown in Figure 15. An RGB color composite of summary parameters for olivine, low-Ca pyroxene, and high-Ca pyroxene suggests that the light-toned unit contains olivine, whereas the dark-toned unit contains high-Ca pyroxene and olivine (Figure 15). An RGB color composite of summary parameters for hydrated minerals was also examined; there is little evidence for hydrated minerals in either unit. Spectra extracted from the light and dark-toned units show a difference in overall albedo, with the dark-toned unit exhibiting ~0.05 lower reflectance across the most of the near-infrared (NIR) range (Figure 15c). The light-toned unit also exhibits a stronger red slope between ~1.0 and 2.6 μm than the dark-toned unit. These CRISM spectra are compared with library spectra of a variety of mafic igneous rocks in Figure 15c. The units do not resemble the laboratory samples selected for comparison; however, there may be contributions from dust or sediment that obscure the true spectral character.

[30] To accentuate spectral features and minimize atmospheric gas absorptions that were not fully removed in the atmospheric correction routine, CRISM data users commonly ratio spectra from units of interest to nearby spectrally "neutral" surfaces, usually meaning a surface with a flat, featureless reflectance spectrum [e.g., *Murchie et al*., 2007]. The CRISM scene which covers the type locality for this stratigraphy contains no such surface. However, we can at least ratio to olivine-poor terrains to confirm the presence of olivine in both units and also to confirm the lack of OH or H_2O vibrational combination/overtone bands (Figure 15d). At first glance, the ratio spectra appear consistent with olivine. However, we note that the reflectance

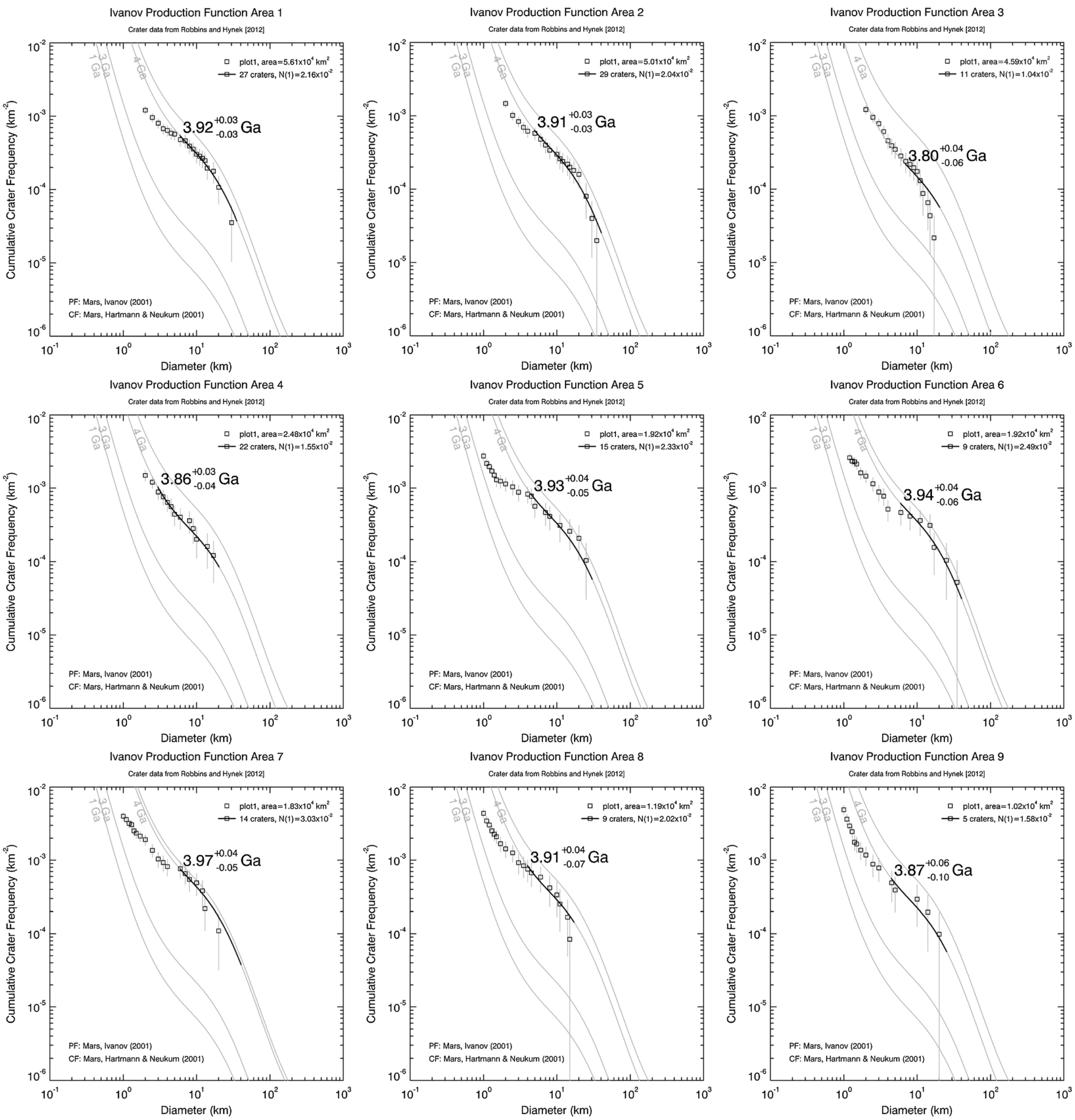

Figure 16. Cumulative size-frequency diagrams for the most areally extensive low-lying ridged plains units showing best fit isochrons (Production Function of [*Ivanov*, 2001]). See also Table 2.

minimum for the light-toned unit is shifted slightly towards longer wavelengths (centered near ~1.25 μm) than the dark-toned unit, and there is an upturn in reflectance going from ~1.25 μm to ~1.0 μm. This suggests that olivine may not be the unique component in the light-toned unit or that perhaps the shift to longer wavelength is due to cation substitution for Fe or Mg in olivine or pyroxene. Alternatively, the mismatch with library spectra may be an artifact of using a non-neutral denominator in the ratio. Recent work presented by *Wray et al*. [2013] suggested that the CRISM spectra of the light-toned unit may be consistent with a felsic rock type with <5% mafic components. The ratio spectrum we derive is consistent with feldspar (Figure 15d); however, a felsic rock type is not consistent with the TES-derived modeled abundances which include ~30% pyroxene. It is possible that subpixel mixing of a felsic and mafic component may be the reason for the discrepancy in interpretation. Additional CRISM images were analyzed and show similar trends as well as similar difficulty of interpretation. The light- and dark-toned units differ only slightly from surroundings, with the light-toned unit having a stronger red slope and higher overall reflectance than the lower, dark-toned unit. Difficulty in interpretation comes from a combination of ratioing to non-neutral surfaces as well as analysis of broad, wide bands. Subtle differences in the denominator spectra change the shape and position of these broad bands,

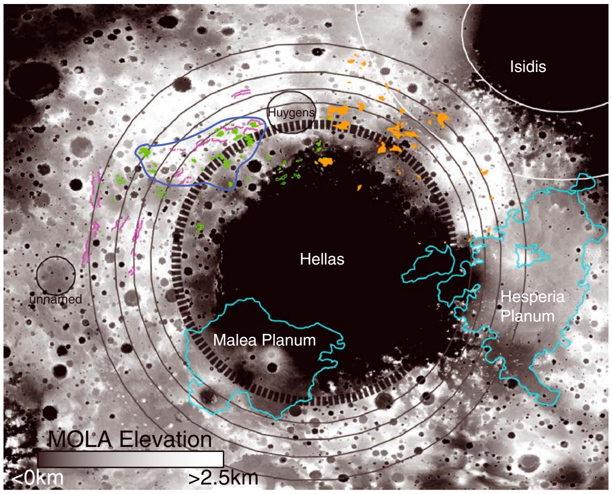

Figure 17. MOLA topography centered on the Hellas basin, showing context of volcanic units mapped in this study and previous studies. Green polygons and purple lines indicate high-TI units and Hellas structures (some of which were mapped by *Wichman and Schultz* [1989]), respectively, as shown in Figure 2b. Blue line outlines the general area where mafic bedrock units are found in this study, which may have a common origin. Black lines are best-fit circles to the Hellas ring structures, for reference. The thick dashed line signifies the main basin scarp [*Wichman and Schultz* [1989]). Cyan outlines show locations of volcanic plains near the rim of Hellas Basin; previous researchers have hypothesized that these plains formed during volcanism enabled by post-impact development of Hellas basin. The white lines show the location of the Isidis crater floor and outer basin scarp from *Wichman and Schultz* [1989]. The orange polygons show locations of mafic rocky units mapped by *Rogers and Fergason* [2011].

making interpretation of the ratio spectra difficult. Further work is needed to understand the visible/near-infrared signatures of these two units.

4.3. Crater Retention Ages

[31] Cumulative size-frequency diagrams were generated, and isochrons were best fit for each of the plains exposures using the methods discussed in section 3.4. Data for all continuous areas were recorded, but only areas with an area greater than 10,000 km^2 are presented because of increasing fitting uncertainty and low numbers of craters (Table 2). Age estimations for the low-lying ridged plains which contain the high-TI units fall in the 3.80–3.98 Ga range with an average age of 3.92 Ga. (Figure 16). Age estimates on the high-TI units only, which were derived from craters down to 250 m diameter (section 3.4), yield ages between 3.71 and 3.94 Ga. However, because of the relatively small number of craters at diameters unaffected by resurfacing (see section 3.4), we favor ages on the older side of this range in good agreement with the ages derived from larger, more areally extensive units (Figure 3c).

4.4. Spatial Association With Hellas Ring Structures

[32] The study region includes a number of ridges and fault-bounded, elongate troughs up to ~100 km wide and ~1000 km long that trend NE-SW or E-W, roughly parallel with the curvature of western Hellas Basin [e.g., *Greeley and Guest*, 1987; *Wichman and Schultz*, 1989; *Tanaka and Leonard*, 1995] (section 2). These troughs do not trace a perfect circle; this may indicate that the Hellas Basin is slightly elongated in the NW-SE direction, as suggested by *Tanaka and Leonard* [1995]. In addition, some of the troughs may be related to the Huygens impact crater, which superposes the Hellas basin scarp. Within the study region, high-TI plains units are not observed westward of the outermost Hellas concentric canyon. Of the total area mapped as "low-lying ridged plains" (which contain rocky exposures), nearly 60% are contained within units that intersect a ring structure (trough or scarp), with some found on the floors of the troughs or partially burying the troughs and others adjacent to scarps. The mapped rocky units are observed both outside and basinward of the main basin scarp (Figure 2b). As described in section 4.1, some of the ridges that crosscut the rocky units are linear and vertically offset not only the rocky units but also the adjacent, degraded plains and massif units by ~200–400 m. Most of these linear ridges are coaligned with the curvature of the basin rim or coincide with the basin scarp, suggesting that they are related to the post-impact basin development. Because the rocky units are deformed by these faults, the ages of the units place a limit on the earliest timing of that tectonic activity (younger than ~3.9 Ga).

5. Discussion and Implications

5.1. Probable Formation Mechanism: Effusive Volcanism

[33] Though all of the rocky exposures share a common characteristic, which is that they are less dominated by sediment than surrounding low-TI surfaces, it is not necessarily expected that they should all share a common formation mechanism or timing of emplacement. Nevertheless, most of the rocky units have crater retention ages (interpreted here as emplacement ages) of ~3.8–4.0 Ga, consistent with their heavily degraded appearance and their modification by wrinkle ridges and faults. Most of the units also exhibit a rugged, massive texture, which suggests structural competence, and lack evidence for fine-scale layering. Finally, most of the units are compositionally distinct from the surrounding low-TI plains, with a higher abundance of mafic minerals and lower abundance of high-silica amorphous or poorly crystalline phases that are likely alteration products.

[34] The preservation of an apparent stratigraphic sequence over long distances suggests a common origin for at least the occurrences where the sequence is observed. The preserved stratigraphy is discontinuously exposed across hundreds of kilometers and is also observed in some crater floors (Figure 2). But what was the process which produced this compositional stratigraphy? The lack of alteration phases or evidence for fine-scale layering does not favor a sedimentary origin. Furthermore, there is no evidence for a compositionally distinct unit in the region that would provide the source of that sediment. It is possible that the light-toned unit represents air fall ash, overlying a dark-toned rocky unit of separate origin. But the unit does not have a friable appearance or morphologies consistent with other likely ash deposits on Mars, such as the Medusa Fossae formation. In addition, the unit does not drape topography and is found exclusively in topographic

lows, which further argues against an air fall origin. A third possibility is that the units represent differentiated impact melt, deposited from either the Hellas impact or other large impact basin. The crater retention ages (if they represent emplacement age) are younger than the Hellas impact event by ~60–260 Myr, depending on which study is cited for the Hellas impact age (*Frey* [2008]: ~4.07 Ga; *Robbins et al.* [2013]: ~4.06 ± 0.02 Ga). The difference in age (particularly for the youngest deposits) would argue against an impact melt origin; however, this does not account for ages influenced by resurfacing and/or the time it would take to cool and solidify the melt. As described above, the units appear to embay higher standing massifs that are likely excavated crustal blocks from the Hellas impact. The units are only found in relative topographic lows and not overlying the higher parts of the massifs, as might be expected for impact melt; however, it is possible that melts would have sloughed off topographic rises while liquid or perhaps were thinner on topographic rises and more easily eroded. Thus, differentiated impact melt remains a possibility, but the evidence in favor of magmatic activity is considered to be stronger (described below).

[35] Two remaining possibilities are that the units represent effusive lavas of varying composition or exposed shallow intrusions. Aside from the massive textures, resistant morphology, and mafic compositions, evidence for an igneous origin comes from the graben floor units, which are thickest in the center of the graben and do not fill the graben floor (Figure 5). This suggests that the source of the material is from the center of the graben floor rather than eroded from the graben walls or blown in from elsewhere and trapped in a topographic low. If intrusive, the different compositions could represent differentiation within the intrusions; alternatively, the light-toned unit represents a thin contact zone between intrusions and overlying material which has since been removed. Between the intrusive and extrusive explanations, the intrusive origin is considered less likely, because of the presence of "ghost" craters observed within the rocky units (Figure 6d). These infilled craters imply burial rather than an intrusive process. It is possible (even likely) that both processes contributed to these units; in any case, each of these processes implies near-surface magmas.

[36] Thus, extrusive volcanism appears to be the most likely origin for these units. The extensive area and rarity of flow fronts implies low viscosity lavas with high effusion rates and large magma volumes, analogous to large igneous provinces on Earth. On Earth, the changing chemical composition associated with members of a flood basalt sequence has been attributed to changing magma sources and/or varying amounts of crustal assimilation. Though the light-toned nature of the upper unit does not seem consistent with basalt, it is possible that there are grain sizes, textural effects, or IR-optically thin coatings that are affecting the overall reflectance of this unit. Furthermore, the actual NIR albedo does not exceed 0.23 (Figure 15), which is dark relative to light-toned aqueous deposits on Mars (e.g. ~0.26 for high-TI sulfate-bearing deposits in Juventae Chasma [*Bishop et al.*, 2009]). The total exposed area of mafic units within the study region is ~42,200 km^2. Using the extent of low-lying ridged plains mapped in MOLA data (dashed polygons in Figure 3c) as a proxy for the true extent of these units, we calculate an area of ~270,700 km^2. This estimate excludes intracrater bedrock deposits, which could be of variable origin. However, we note that many, if not all, of the intracrater bedrock may have formed in a similar manner, and thus these areal estimates are certainly lower limits. The total bedrock unit thickness, while variable, is estimated not to exceed ~200 m (section 4.1). Using this thickness and the total area of bedrock-containing, low-lying ridged plains, we can place an upper limit on the volume of extruded material to be 56,000 km^3. This estimate does not account for the large volume of magma that likely cooled at depth, nor does it account for the crater floor exposures that may have a common origin to the intercrater plains and graben floor exposures (for example, Figures 8f and 9c). The extensive area and high magma volumes are analogous to large igneous provinces on Earth; however, the discontinuous outcrop pattern is different than the broad expanses of continuous lavas observed in terrestrial flood basalt provinces. This pattern can be attributed to partial burial by impacts and other sediments, as well as the fact that the crust may have been too thick in this region to achieve high enough lava volumes at the surface to completely bury the high-standing massifs and ridges.

5.2. Comparison With Martian Meteorites and Other Volcanic Units

[37] At ~3.8–4.0 Ga old, these are some of the oldest known volcanic units exposed at the surface of Mars and thus provide important data points for comparisons with younger volcanic terrains and Martian meteorites. Because of the relatively high plagioclase/pyroxene ratios, the Noachis units are dissimilar from most shergottites [e.g., *McSween* 2008], except for Los Angeles [*Rubin et al.*, 2000]. The modal mineralogy of the light-toned unit is broadly similar to Los Angeles (~44% maskelynitized plagioclase, ~44% pyroxene, and ~1–5% olivine) [*Rubin et al.*, 2000], suggesting Los Angeles may have a common history with some of these units. The reportedly young crystallization age of Los Angeles (~165 Ma [*Nyquist et al.*, 2001]) excludes the Noachis region from being a source region of this meteorite, however.

[38] Figure 13 compares the TES-derived spectra from the dark- and light-toned units with regionally derived TES surface units, as well as other likely igneous units in Gusev crater and Ares Vallis. Regional studies of low-albedo surfaces using TES data were carried out by *Rogers et al.* [2007] and *Rogers and Christensen* [2007], with major mineralogical distinctions observed in Acidalia Planitia ("group 1"), Syrtis Major ("group 2"), cratered highlands including Tyrrhena, Cimmeria, and Meridiani ("group 3"), and Thaumasia/Aonia Plana ("group 4"). Of these groups, the units presented here are most similar to Syrtis Major, both in spectral shape and derived mineralogy, but the lower unit exhibits lower emissivity near ~900 cm^{-1} relative to ~1100 cm^{-1}, and there are slight differences in the shapes and positions of long wavelength absorptions for both units in comparison to Syrtis. In addition, the Noachis units exhibit slightly higher olivine abundance than Syrtis. Bedrock in the floor of Syrtis Major's northern caldera, Nili Patera, was examined by *Christensen et al.* [2005] with TES and THEMIS data. The derived modal mineralogy for Nili Patera is broadly similar to Syrtis Major lavas and to the light-toned unit presented here. The Mars Exploration Rover Spirit examined several rock types with the Miniature Thermal Emission Spectrometer (Mini-TES) in Gusev Crater [*Ruff et al.*, 2006; *Hamilton and Ruff*, 2012].

Adirondack-class basalts, which dominate the floor of Gusev, have a high olivine component (up to 30%) and are not similar in spectral shape to Noachis units. Wishstone class rocks have a strong plagioclase component, but the abundance is much higher than either of the Noachis units, and the features of plagioclase are clearly visible in the thermal emission spectra [*Ruff et al*., 2006], unlike the Noachis units. Bedrock units in Nili Fossae [*Hamilton and Christensen*, 2005], Ares Vallis [*Rogers et al*., 2005], and Ganges Chasma [*Edwards et al*., 2008] have been examined in detail with TES and THEMIS data; however, all are strongly enriched in olivine relative to Noachis units (Ares Vallis shown in Figure 13). Thus, we conclude that the Noachis units are distinct from previously characterized thermal infrared (TIR) spectral units on Mars; the closest matches would be Syrtis Major lavas and the Nili Patera caldera floor but with an enrichment of ~5–10% olivine.

5.3. Magma Ascent Likely Enabled by Hellas-Related Structures and Fractures

[39] Volcanism at Hesperia Planum, Malea Planum, Hadriaca Patera, and Tyrrhena Patera has been previously suggested to be related to Hellas formation and tectonic development [*Peterson*, 1978; *Schultz and Glicken*, 1979; *Wichman and Schultz*, 1989]. The spatial association of the "rim" volcanic plains with Hellas rings led some researchers to speculate that lithospheric flexure caused by basin loading enabled magma ascent in these areas, beginning around ~3.8 Ga. In some areas, volcanism continued through the early Hesperian, forming the vast ridged plains of Hesperian and Malea Plana. MGS topography and gravity observations over Hellas are not consistent with significant gravitational mass excess [*Smith et al*., 1999], suggesting that flexure from basin loading is unlikely. However, we expect that the impact event would have led to extensive subsurface fracturing. Between this fracturing and the formation of the Hellas circumferential graben during transit cavity collapse, we surmise that the Hellas impact would have formed an extensive network of conduits that allowed melts to more easily reach the surface.

[40] As described above, the rocky units in northern Noachis Terra show spatial association with troughs and ridges related to the Hellas impact. Crosscutting relationships indicate that the rocky units were emplaced after the formation of the troughs but prior to ridge formation. Thus, we propose that these units were part of the basin-related volcanic activity proposed for Hesperia and Malea Planum by previous researchers. If correct, this study suggests that the timing of onset of the basin-related volcanism may have been earlier than previously thought (~3.98 Ga, versus ~3.8 Ga for Tyrrhena and Hadriaca Paterae [*Williams et al*., 2010]). Also, these observations suggest that some of the basin volcanism may have been fissure-fed, similar to lunar mare, in addition to the construct-building styles of volcanism found at Hadriaca and Tyrrhena Paterae.

[41] It is not clear what role the fracturing and/or extensional tectonics played in generation of melt in this region. There are no aspects of the modal mineralogy (e.g., a komatiite or picrite) that requires invoking exceptionally high degrees of partial melting or high mantle temperatures. Thermal evolution models allow for some melt at the base of the crust during this time period [*Hauck and Phillips*, 2002; *Schumacher and Breuer*, 2007] particularly if located under areas of thickened crust [*Schumacher and Breuer*, 2007]. Thus, there is no need to call for a decompression melting via extensional tectonics, though this process may have played a role in melt generation. Finally, though the Hellas impact itself could have generated the partial melts needed to form these units [*Marinova et al*., 2011], these melts would likely have migrated to the surface in very short timeframes ($<10^2$ years, calculated using relationships shown in *Melosh* [2011]). This is not consistent with the estimated difference in timing between the Hellas impact and the emplacement of these units (~60–260 Myr, section 5.1). A more likely explanation is that mantle temperatures were still high enough during this time period such that melts would have been present at the base of this crust. Fracturing and extensional tectonics associated with the formation and development of Hellas Basin allowed this melt to ascend through very thick crust, beginning at least ~60 Myr after the impact event.

[42] If Hellas basin tectonics are responsible for rim volcanism in northern Noachis (this study), Hesperia and Malea (previous studies, e.g., *Peterson* [1978]; *Schultz and Glicken* [1979]; and *Wichman and Schultz* [1989]), one might expect to see evidence of this volcanism in other circum-Hellas terrains such as Iapygia Terra to the north of Hellas and Tyrrhena Terra to the northeast. *Rogers and Fergason* [2011], *Loizeau et al*. [2012], and *Ody et al*. [2012a, 2012b] did report the presence of mafic rocky exposures in Tyrrhena and Iapygia Terrae (Figure 17) and speculated that they were volcanic deposits. It is possible that these units are also Hellas basin-related rim volcanics; in addition, the Isidis Basin to the north may have also played a role in enabling volcanism in this region. Mafic rocky units, while rare, do occur in other parts of the Martian highlands relatively far from large impact basins. In those regions, other mechanisms may be needed to explain their origin, such as a mantle plume [e.g., *Hynek et al*., 2011].

5.4. Implications for Climate During the Mid-Noachian to Late Noachian

[43] Evidence for water-rock interactions in the Noachian comes from fluvial morphologies on crater rims, ejecta, and plains [*Craddock and Howard*, 2002] as well as phyllosilicate minerals found in the surface and subsurface in Noachian terrains [e.g., *Ehlmann et al*., 2011]. Many of the crater-exposed phyllosilicate minerals are higher-temperature phyllosilicates such as prehnite and chlorite and likely formed in hydrothermal environments [e.g., *Ehlmann et al*., 2011; *Loizeau et al*., 2012].

[44] Volcanic activity can play a major role in temporarily affecting Martian climate as well as hydrothermal processes. Current estimates of the water content of the martian mantle from kaersutite melt inclusions in the Chassigny meteorite range from 130 to 250 ppm [*McCubbin et al*., 2010]. Assuming degree of partial melting between 5 and 15%, this yields water contents in the melt of 200–1200 ppm. Thus, for the units mapped in this region, total water brought to the surface could have ranged between ~11 and 68 km^3. Globally, this is a small volume, however locally, it is substantial. The combination of heat and water could have led to hydrothermal environments and possibly precipitation in this region, conducive to clay formation and habitability in both the surface and subsurface.

[45] Most valley networks on Mars likely formed between ~3.8 and 3.6 Ga [*Howard et al*., 2005; *Irwin et al*., 2005; *Fassett and Head*, 2008; *Hynek et al*., 2010], which slightly postdates the ages of our mapped units. However, a minor fraction may have formed prior to ~3.8 Ga [*Fassett and Head*, 2008]. Furthermore, ancient craters also show evidence of fluvial modification throughout the Noachian [*Craddock and Howard*, 2002]. The mid-Noachian to Late Noachian crater retention age of mapped units in this study coincides with the proposed timing of the earliest valley network formation and some fluvially modified craters; thus, we infer that volcanism may have temporarily influenced Martian climate to allow formation of these fluvial features. At the surface, Mars may have generally remained cold throughout the Noachian, with punctuated stages of precipitation related to Tharsis activity and indirectly related to multi-ring impact basins via volcanism through subsurface fracturing. This volcanism would have led to hydrothermal activity and mineralization in the subsurface. Thus, we conclude that multi-ring impact basin formation on early Mars may have played a role in Martian climate that has perhaps been underestimated in the past.

6. Conclusions

[46] 1. Rocky expanses of mafic material in Noachis Terra are interpreted as effusive volcanic plains on the basis of broad areal extent, structural competence, association with topographic lows, distinct mineralogy from regolith, and lack of sedimentary textures or minerals associated with aqueous processes. These units are heavily degraded and partially buried by impact ejecta and other sediment. The crater model ages range from ~3.8 to 3.98 Ga, with an average of ~3.9 Ga.

[47] 2. Some rocky expanses contain at least two compositionally distinct units. The upper unit is relatively light toned and exhibits a higher plagioclase/pyroxene ratio than the lower, dark-toned unit. Both units exhibit ~10% olivine enrichment compared to surrounding regolith and lack high-silica phases. These units most likely represent compositionally distinct members of a flood basalt sequence.

[48] 3. These volcanic plains are found in association with Hellas ring structures, where the westward extent of these units does not reach beyond the outermost ring structure. Some mafic rocky units are found on the floors of Hellas circumferential graben, and others partially bury the ring structures. Fracturing associated with the Hellas impact may have enabled magmas to ascend from the base of the crust in the circum-Hellas region. Basin-related rim volcanism has been suggested by previous researchers for Hesperia and Malea Plana [*Schultz and Glicken*, 1979] and is further supported by this work. The onset of Hellas-related volcanism is further constrained by this work to have occurred as early as ~3.98 Ga, within ~60 Myr of the Hellas impact.

[49] 4. Identification of these units as volcanic materials extends previous estimates for volcanic volumes, which affects estimates of the volume and timing of outgassed volatiles. Though the estimated volume increase is minor, the local effects could have been significant. Heat and volatiles brought to the surface may have temporarily affected local climate, and conditions may have been conducive for subsurface aqueous mineralization and crater degradation by fluvial processes.

[50] 5. The Noachis units represent some of the earliest preserved basalts accessible by remote sensing. The relatively high plagioclase/pyroxene ratio makes them dissimilar to most Martian meteorites, with the exception of Los Angeles. Compared to other regionally or locally derived spectral units on Mars, the Noachis units are most similar to Syrtis Major lavas, except for a small (10%) enrichment in olivine.

[51] 6. Rocky mafic units have been identified in Iapygia and Tyrrhena Terra in previous studies [*Rogers and Fergason*, 2011]. These units are found within the ring structures of Hellas and/or Isidis (ring structures overlap) and may also represent basin-related volcanism. Thus, the role of multi-ring impact basins providing a spatial control on Martian highlands volcanism, and subsurface mineralization may have been underestimated in the past.

[52] **Acknowledgments.** This work was partially supported by the Mars Odyssey project, NASA Planetary Geology and Geophysics program, and the NASA Mars Data Analysis program. We thank the Mars Odyssey and Mars Reconnaissance Orbiter teams for their efforts, which have resulted in valuable data products and analysis tools. We thank Vicky Hamilton and Steve Ruff for lending the Mini-TES spectra of the Adirondack and Wishstone class rocks at Gusev crater. The ideas in this paper were better developed through conversations with Hanna Nekvasil. We are grateful to Bethany Ehlmann and Kimberly Seelos for thorough, insightful reviews.

References

Bandfield, J. L. (2002), Global mineral distributions on Mars, *J. Geophys. Res.*, *107*(E6), 5042, doi:10.1029/2001JE001510.
Bandfield, J. L., V. E. Hamilton, and P. R. Christensen (2000), A global view of Martian surface compositions from MGS-TES, *Science*, *287*(5458), 1626–1630.
Bandfield, J. L., D. Rogers, M. D. Smith, and P. R. Christensen (2004), Atmospheric correction and surface spectral unit mapping using Thermal Emission Imaging System data, *J. Geophys. Res.*, *109*(E10), E10008, doi:10.1029/2004JE002289.
Bishop, J. L., et al. (2009), Mineralogy of Juventae Chasma: Sulfates in the light-toned mounds, mafic minerals in the bedrock, and hydrated silica and hydroxylated ferric sulfate on the plateau, *J Geophys Res.*, *114* (E2), doi:10.1029/2009JE003352.
Broxton, M. J., and L. J. Edwards, (2008), The Ames Stereo Pipeline: Automated 3D surface reconstruction from orbital imagery, *Lunar and Planetary Science Conference 39*, abstract #2419.
Christensen, P. R., and H. J. Moore (1992), The Martian surface layer, in *Mars*, edited by H. H. Kieffer, B. M. Jakosky, C. W. Snyder, and M. S. Matthews, pp. 686–729, Univ. of Arizona Press, Tuscon, Ariz.
Christensen, P. R., et al. (2004), The Thermal Emission Imaging System (THEMIS) for the Mars 2001 Odyssey Mission, *Space Sci Rev,110*(1–2) 85–130.
Christensen, P. R., et al. (2005), Evidence for igneous diversity and magmatic evolution on Mars from infrared spectral observations, *Nature*, *436*(7052), 504–509, doi:10.1038/nature03639.
Christensen, P. R., E. Engle, S. Anwar, S. Dickenshied, D. Noss, N. Gorelick, M. Weiss-Malik (2009), JMARS—A Planetary GIS, American Geophysical Union, Fall Meeting 2009, abstract #IN22A-06, http://adsabs.harvard.edu/abs/2009AGUFMIN22A..06C
Craddock, R. A., and A. D. Howard (2002), The case for rainfall on a warm, wet early Mars, *J. Geophys. Res.*, *107*(E11), 5111, doi:10.1029/2001JE001505.
Cruikshank, D. P., W. K. Hartmann, and C. A. Wood (1973), Moon: "Ghost" craters formed during mare filling, *Moon*, *7*440–452, doi:10.1007/BF00564645.
Edwards, C. S., P. R. Christensen, and V. E. Hamilton (2008), Evidence for extensive olivine-rich basalt bedrock outcrops in Ganges and Eos chasmas, Mars, *J. Geophys. Res.*, *113*(E11), E11003, doi:10.1029/2008JE003091.
Edwards, C. S., J. L. Bandfield, P. R. Christensen, and R. L. Fergason (2009), Global distribution of bedrock exposures on Mars using THEMIS high-resolution thermal inertia, *J. Geophys. Res.*, *114*, E11001, doi:10.1029/2009JE003363.
Edwards, C. S., A. D. Rogers, J. L. Bandfield, and P. R. Christensen (2010), Volcanic Origin of Flat Floored, Bedrock Containing Craters on Mars, in *41st Lunar and Planetary Science Conference*, Abstract #1543, Lunar and Planetary Institute, Houston, Tex.

Edwards, C. S., K. J. Nowicki, P. R. Christensen, J. Hill, N. Gorelick, and K. Murray (2011), Mosaicking of global planetary image datasets: 1. Techniques and data processing for Thermal Emission Imaging System (THEMIS) multi-spectral data, *J. Geophys. Res.*, *116*(E10), E10008, doi:10.1029/2010JE003755.

Edwards, C. S., J. L. Bandfield, P. R. Christensen, and A. D. Rogers (2013), The Formation of Infilled Craters by Impact Induced Decompression Melting of the Martian Mantle. *44th Lunar and Planetary Science Conference*, Abstract #2153. Available from: http://www.lpi.usra.edu/meetings/lpsc2013/pdf/2153.pdf.

Ehlmann, B. L., J. F. Mustard, S. L. Murchie, J.-P. Bibring, A. Meunier, A. Fraeman, and Y. Langevin (2011), Subsurface water and clay mineral formation during the early history of Mars, *Nature*, *479*(7371), 53–60, doi:10.1038/nature10582.

Fassett, C. I., and J. W. Head (2008), The timing of martian valley network activity: Constraints from buffered crater counting, *Icarus*, *195*(1), 61–89, doi:10.1016/j.icarus.2007.12.009.

Fergason, R. L., P. R. Christensen, and H. H. Kieffer (2006), High-resolution thermal inertia derived from the Thermal Emission Imaging System (THEMIS): Thermal model and applications, *J. Geophys. Res.*, *111*, E12004.

French, B. M. (1998), *Traces of Catastrophe: A Handbook of Shock-Metamorphic Effects, Terrestrial Meteorite Impact Structures*, p. 97, Smithsonian Institution, Washington D.C.

Frey, H. V. (2008), Ages of very large impact basins on Mars: Implications for the late heavy bombardment in the inner solar system, *Geophys. Res. Lett.*, *35*, L13203, doi:10.1029/2008GL033515.

Gillespie, A. R. (1992), Enhancement of multispectral thermal infrared images—Decorrelation contrast stretching, *Remote Sens. Environ.*, *42*(2), 147–155.

Greeley, R., and J. E. Guest (1987), Geologic map of the eastern equatorial region of Mars.

Hamilton, V. E., and P. R. Christensen (2005), Evidence for extensive, olivine-rich bedrock on Mars, *Geology*, *33*(6), 433–436.

Hamilton, V. E., and S. W. Ruff (2012), Distribution and characteristics of Adirondack-class basalt as observed by Mini-TES in Gusev crater, Mars and its possible volcanic source, *Icarus*, *218*(2), 917–949, doi:10.1016/j.icarus.2012.01.011.

Hartmann, W. K. (2005), Martian cratering 8: Isochron refinement and the chronology of Mars, *Icarus*, *174*, 294–320.

Hartmann, W. K., and G. Neukum (2001), Cratering chronology and the evolution of Mars, *Space Sci. Rev.*, *96*, 165–194, doi:10.1023/A:1011945222010.

Hauck, S. A., and R. J. Phillips (2002), Thermal and crustal evolution of Mars: v. 107.

Head, J. W., L. Wilson, J. Dickson, and G. Neukum (2006), The Huygens-Hellas giant dike system on Mars: Implications for Late Noachian-Early Hesperian volcanic resurfacing and climatic evolution, *Geology*, *34*(4), 285–288, Retrieved from < Go to ISI>://000236726900016

Howard, A. D., J. M. Moore, and R. P. Irwin (2005), An intense terminal epoch of widespread fluvial activity on early Mars: 1. Valley network incision and associated deposits, *J. Geophys. Res.*, *110*, E12S14, doi:10.1029/2005JE002459.

Hynek, B. M., M. Beach, and M. R. T. Hoke (2010), Updated global map of Martian valley networks and implications for climate and hydrologic processes, *J. Geophys. Res.*, *115*, E09008, doi:10.1029/2009JE003548.

Hynek, B. M., S. J. Robbins, O. Šrámek, and S. J. Zhong (2011), Geological evidence for a migrating Tharsis plume on early Mars, *Earth Planet. Sci. Lett.*, *310*(3–4), 327–333.

Irwin, R. P., A. D. Howard, R. A. Craddock, and J. M. Moore (2005), An intense terminal epoch of widespread fluvial activity on early Mars: 2. Increased runoff and paleolake development, *J. Geophys. Res.*, *110*, E12S15, doi:10.1029/2005JE002460.

Ivanov, B. A. (2001), Mars/Moon cratering rate ratio estimates, *Space Sci. Rev.*, *96*, 87–104, doi:10.1023/A:1011941121102.

Kieffer, H. H. (2013), Thermal model for analysis of Mars infrared mapping, *J. Geophys. Res. Planets*, *118*, 451–470, doi:10.1029/2012JE004164.

Kieffer, H. H., T. Z. Martin, A. B. Peterfreund, B. M. Jakosky, E. D. Miner, and F. D. Palluconi (1977), Thermal and albedo mapping of Mars during the Viking primary mission, *J. Geophys. Res.*, *82*, 4249–4291.

Klimczak, C., et al. (2012), Deformation associated with ghost craters and basins in volcanic smooth plains on Mercury: Strain analysis and implications for plains evolution, *J. Geophys. Res.*, *117*, E00L03, doi:10.1029/2012JE004100.

Kneissl, T., S. van Gasselt, and G. Neukum (2011), Map-projection independent crater size-frequency determination in GIS environments: New software tool for ArcGIS, *Planet. Space Sci.*, *59*, 1243–1254, doi:10.1016/j.pss.2010.03.015.

Koeppen, W. C., and V. E. Hamilton (2008), Global distribution, composition, and abundance of olivine on the surface of Mars from thermal infrared data, *J. Geophys. Res.*, *113*, E05001, doi:10.1029/2007JE002984.

Loizeau, D., et al. (2012), Characterization of hydrated silicate-bearing outcrops in Tyrrhena Terra, Mars: Implications to the alteration history of Mars, *Icarus*, *219*(1), 476–497, doi:10.1016/j.icarus.2012.03.017.

Malin, M. C. (1976), Nature and origin of intercrater plains on Mars. In: Studies of the surface morphology of Mars, Ph.D. dissertation, California Institute of Technolgy.

Malin, M. C., et al. (2007), Context Camera Investigation on board the Mars Reconnaissance Orbiter, *J. Geophys. Res.*, *112*(E5), 25.

Marinova, M. M., O. Aharonson, and E. Asphaug (2011), Geophysical consequences of planetary-scale impacts into a Mars-like planet, *Icarus*, *211*(2), 960–985, doi:10.1016/j.icarus.2010.10.032.

McCubbin, F. M., A. Smirnov, H. Nekvasil, J. Wang, E. Hauri, and D. H. Lindsley (2010), Hydrous magmatism on Mars: A source of water for the surface and subsurface during the Amazonian, *Earth Planet. Sci. Lett.*, *292*(1–2), 132–138, doi:10.1016/j.epsl.2010.01.028.

McDowell, M. L., and V. E. Hamilton (2007), Geologic characteristics of relatively high thermal inertia intracrater deposits in southwestern Margaritifer Terra, Mars, *J. Geophys. Res.*, *112*, E12001, doi:10.1029/2007JE002925.

McEwen, A. S., et al. (2007), Mars Reconnaissance Orbiter's High Resolution Imaging Science Experiment (HiRISE), *J. Geophys. Res.*, *112*(E5), 40.

McGuire, P. C., et al. (2009), An improvement to the volcano-scan algorithm for atmospheric correction of CRISM and OMEGA spectral data, *Planet. Space Sci.*, *57*(7), 809–815.

McKinnon, W. B., and H. J. Melosh (1980), Evolution of planetary lithospheres—Evidence from multiringed structures on Ganymede and Callisto, *Icarus*, *44*(2), 454–471.

McSween, H. Y. (2008), Martian meteorites as crustal samples, in *The Martian Surface*, edited by J. F. Bell, III, pp. 383–396, Cambridge Univ. Press, New York.

Mellon, M. T., B. M. Jakosky, H. H. Kieffer, and P. R. Christensen (2000), High-resolution thermal inertia mapping from the Mars Global Surveyor Thermal Emission Spectrometer, *Icarus*, *148*(2), 437–455.

Melosh, H. J. (2011), *Planetary Surface Processes*, pp. 500, Cambridge University Press, New York.

Mest, S. C., and D. A. Crown (2005), Millochau crater, Mars: Infilling and erosion of an ancient highland impact crater, *Icarus*, *175*(2), 335–359, doi:10.1016/j.icarus.2004.12.008.

Michael, G. G., and G. Neukum (2010), Planetary surface dating from crater size–frequency distribution measurements: Partial resurfacing events and statistical age uncertainty, *Earth Planet. Sci. Lett.*, *294*(3–4), 223–229, doi:10.1016/j.epsl.2009.12.041.

Michael, G. G.,T. Platz, T. Kneissl, and N. Schmedemann (2012), Planetary surface dating from crater size-frequency distribution measurements: Spatial randomness and clustering, *Icarus*, *218*(1), 169–177.

Moratto, Z. M., M. J. Broxton, R. A. Beyer, M. Lundy, and K. Husmann, (2010), Ames Stereo Pipeline, NASA's open source automated stereogrammetry software, *Lunar and Planetary Science Conference 41,* Abstract #2364.

Murchie, S., et al. (2007), Compact reconnaissance Imaging Spectrometer for Mars (CRISM) on Mars Reconnaissance Orbiter (MRO), *J. Geophys. Res.*, *112*(E5), E05S03, doi:10.1029/2006JE002682.

Neumann, G. A., M. T. Zuber, M. A. Wieczorek, P. J. McGovern, F. G. Lemoine, and D. E. Smith (2004), Crustal structure of Mars from gravity and topography, *J. Geophys. Res.*, *109*, E08002, doi:10.1029/2004JE002262.

Nimmo, F., and K. Tanaka (2005), Early crustal evolution of Mars 1, *Annu. Rev. Earth Planet. Sci.*, *33*(1), 133–161, doi:10.1146/annurev.earth.33.092203.122637.

Nyquist, L. E., D. D. Bogard, C. Y. Shih, A. Greshake, D. Stoffler, and O. Eugster (2001), Ages and geologic histories of Martian meteorites, *Space Sci. Rev.*, *96*(1–4), 105–164. Retrieved from < Go to ISI>://000171150700005

Ody, A., et al. (2012a), Global maps of anhydrous minerals at the surface of Mars from OMEGA/MEx, *J. Geophys. Res.*, *117*, E00J14, doi:10.1029/2012JE004117.

Ody, A., F. Poulet, J.-P. Bibring, D. Loizeau, J. Carter, B. Gondet, and Y. Langevin (2012b), Global investigation of olivine on Mars: Insights into crust and mantle compositions, *J. Geophys. Res.*, *118*, doi:10.1029/2012JE004149.

Pelkey, S. M., et al. (2007), CRISM multispectral summary products: Parameterizing mineral diversity on Mars from reflectance, *J. Geophys. Res.*, *112*(E08), E08S14.

Peterson, J. E. (1978), Volcanism in the Noachis-Hellas region of Mars, 2, *Proc. Lunar Planet Sci. Conf.*, *9*, 3411–3432.

Plescia, J. B., and M. P. Golombek (1986), Origin of planetary wrinkle ridges based on the study of terrestrial analog, *Geol. Soc. Am. Bull.*, *97*(11), 1289–1299.

Poulet, F., et al. (2007), Martian surface mineralogy from Observatoire pour la Minéralogie, l'Eau, les Glaces et l'Activité on board the Mars Express spacecraft (OMEGA/MEx): Global mineral maps, *J. Geophys. Res.*, *112*(E8), E08S02, doi:10.1029/2006JE002840.

Robbins, S. J., and B. M. Hynek (2013), A new global database of Mars impact craters ≥1 km: 1. Database creation, properties, and parameters, *J. Geophys. Res.*, *117*, E05004, doi:10.1029/2011JE003966.

Robbins, S. J., B. M. Hynek, R. J. Lillis, and W. F. Bottke (2013), Large impact crater histories of Mars: The effect of different model crater age techniques, *Icarus*, *225*(1), 173–184, doi:10.1016/j.icarus.2013.03.019, in press.

Rogers, A. D., and O. Aharonson (2008), Mineralogical composition of sands in Meridiani Planum determined from MER data and comparison to orbital measurements, *J. Geophys. Res.*, E06S14, doi:10.1029/2007JE002995.

Rogers, A. D., and P. R. Christensen (2007), Surface mineralogy of Martian low-albedo regions from MGS-TES data: Implications for upper crustal evolution and surface alteration, *J. Geophys. Res.*, *112*, E01003, doi:10.1029/2006JE002727.

Rogers, A. D., and R. L. Fergason (2011), Regional-scale stratigraphy of surface units in Tyrrhena and Iapygia Terrae, Mars: Insights into highland crustal evolution and alteration history, *J. Geophys. Res.*, *116*, E08005, doi:10.1029/2010JE003772.

Rogers, A. D., P. R. Christensen, and J. L. Bandfield (2005), Compositional heterogeneity of the ancient Martian crust: Surface analysis of Ares Vallis bedrock with THEMIS and TES data, *J. Geophys. Res.*, *110*, E05010, doi:10.1029/2005JE002399.

Rogers, A. D., J. L. Bandfield, and P. R. Christensen (2007), Global spectral classification of Martian low-albedo regions with Mars Global Surveyor Thermal Emission Spectrometer (MGS-TES) data, *J. Geophys. Res.*, *112*, E02004, doi:10.1029/2006JE002726.

Rogers, A. D., O. Aharonson, and J. L. Bandfield (2009), Geologic context of in situ rocky exposures in Mare Serpentis, Mars: Implications for crust and regolith evolution in the cratered highlands, *Icarus*, *200*(2), 446–462, doi:10.1016/j.icarus.2008.11.026.

Rubin, A. E., et al. (2000), Los Angeles: The most differentiated basaltic Martian meteorite, *Geology*, *28*(11), 1011–1014. Retrieved from < Go to ISI>://000165277900013

Ruff, S. W., P. R. Christensen, D. L. Blaney, W. H. Farrand, J. R. Johnson, J. R. Michalski, J. E. Moersch, S. P. Wright, and S. Squyres (2006), The rocks of Gusev Crater as viewed by the Mini-TES instrument, *J. Geophys. Res.*, *111*, E12S18, doi:10.1029/2006JE002747.

Salisbury, J. W., L. S. Walter, N. Vergo, and D. M. D'Aria (1991), *Infrared (2.1–25 Micrometers) Spectra of Minerals*, 294 pp., Johns Hopkins Univ. Press.

Salvatore, M. R., J. F. Mustard, M. B. Wyatt, and S. L. Murchie (2010), Definitive evidence of Hesperian basalt in Acidalia and Chryse planitiae, *J. Geophys. Res.*, *115*.

Schultz, P. H., and H. Glicken (1979), Impact crater and basin control of igneous processes on Mars, *J. Geophys. Res.*, *84*(B14), 8033, doi:10.1029/JB084iB14p08033.

Schumacher, S., and D. Breuer (2007), An alternative mechanism for recent volcanism on Mars, *Geophys. Res. Lett.*, *34*, L14202, doi:10.1029/2007GL030083.

Smith, D. E., et al. (1999), The global topography of Mars and implications for surface evolution, *Science*, *284*(5419), 1495–1503.

Smith, D. E., et al. (1999), Mars Orbiter Laser Altimeter: Experiment summary after the first year of global mapping of Mars, *J. Geophys. Res.*, *106*(E10), 23689–23722.

Tanaka, K. L., and G. J. Leonard (1995), Geology and landscape evolution of the Hellas region of Mars, *J. Geophys. Res.*, *100*(E3), 5407–5432, doi:10.1029/94JE02804.

Tanaka, K. L., N. K. Isbell, D. H. Scott, R. Greeley, and J. E. Guest (1988), The resurfacing history of Mars: A synthesis of digitized, Viking-based geology, *Proc. Lunar Sci. Conf.*, *18*, 665–678.

Wichman, R. W., and P. H. Schultz (1989), Sequence and mechanisms of deformation around the Hellas and Isidis impact basins on Mars, *J. Geophys. Res.*, *94*(B12), 17333–17357, doi:10.1029/JB094iB12p17333.

Williams, D. A., R. Greeley, L. Manfredi, J. Raitala, and G. Neukum (2010), The Circum-Hellas Volcanic Province, Mars: Assessment of wrinkle-ridged plains, *Earth Planet. Sci. Lett.*, *294*(3–4), 492–505, doi:10.1016/j.epsl.2009.10.007.

Wray, J. J., S. T. Hansen, J. Dufek, G. A. Swayze, S. L. Murchie, F. P. Seelos, J. R. Skok, R. P. I. Irwin, and M. S. Ghiorso (2013), Infrared spectral identification of unusually feldspar-rich rocks on Mars, *44th Lunar and Planetary Science Conference*, Abstract #3065. Available from: http://www.lpi.usra.edu/meetings/lpsc2013/pdf/3065.pdf.

Zuber, M. T., et al. (2000), Internal structure and early thermal evolution of Mars from Mars Global Surveyor topography and gravity, *Science*, *287*(5459), 1788–1793.